OPTICAL PROPERTIES OF ASYMMETRIC DOUBLE QUANTUM WELLS AND OPTIMIZATION FOR OPTICAL MODULATORS

A Dissertation
Presented to
The Academic Faculty

by

Dong Kwon Kim

In Partial Fulfillment
of the Requirements for the Degree
Doctor of Philosophy in the
School of Electrical and Computer Engineering

Georgia Institute of Technology
May 2008

Copyright © Dong Kwon Kim 2008

OPTICAL PROPERTIES OF ASYMMETRIC DOUBLE QUANTUM WELLS AND OPTIMIZATION FOR OPTICAL MODULATORS

Approved by:

Dr. David S. Citrin, Advisor
School of Electrical and Computer Engineering
Georgia Institute of Technology

Dr. William T. Rhodes
School of Electrical and Computer Engineering
Georgia Institute of Technology

Dr. Thomas K. Gaylord
School of Electrical and Computer Engineering
Georgia Institute of Technology

Dr. Russell D. Dupuis
School of Electrical and Computer Engineering
Georgia Institute of Technology

Dr. Zhuomin Zhang
School of Mechanical Engineering
Georgia Institute of Technology

Date Approved: February 29, 2008

To my parents
Young Ok Park and Moon Chang Kim
and
to my wife
Kyung Ok Kim

ACKNOWLEDGEMENTS

I am deeply indebted to my advisor, Dr. David S. Citrin, not only academically but also in every aspect of my life after I met him. I am thankful to him for giving me the opportunities to indulge myself in this wonderfully intriguing research field, guiding me to the right research direction, and sharing his deep insights into physics. He also gave me chances to travel all around the northern hemisphere including one year of stay in France where he and his wife, Dr. Alka Citrin, took a special care of me and my family.

I am thankful to Dr. Abdalla Ougazzaden for sharing his valuable experimental experience on InP-based quantum wells, to Dr. Stephen Hughes for giving me the advices on the numerical techniques in calculating excitons, and to Dr. Douglas R. Denison for the discussions on high-sensitivity field detectors. I thank the current and former group members for their help and friendship.

I would like to thank Drs. William T. Rhodes, Thomas K. Gaylord, and Russell D. Dupuis for their time on reading and commenting both of my proposal and dissertation and Dr. Zhuomin Zhang for serving on my dissertation committee.

I appreciate my wife's support and endeavor during my PhD period. Finally I cannot thank my parents enough for their endless support and love.

TABLE OF CONTENTS

Page

ACKNOWLEDGEMENTS iv

LIST OF TABLES vii

LIST OF FIGURES viii

SUMMARY xii

CHAPTER

1 Introduction 1

2 Linear optical properties of quantum wells 9

2.1 Material parameters of alloys and band-edge profiles 10

2.1.1 Material parameters of alloys 10

2.1.2 Band-edge profiles 14

2.2 Subbands in quantum wells 14

2.2.1 Conduction subbands 15

2.2.2 Valence subbands 16

2.3 Excitons in quantum wells 21

2.4 Linear optical susceptibilities in quantum wells 25

2.5 Line broadenings 29

3 Electric-field-induced mixing of excitons in asymmetric double quantum wells 34

3.1 Mixing of excitons originating in different subband pairs 37

3.2 Analysis of exciton mixing in ADQWs 39

3.2.1 Effect of exciton mixing in strongly and weakly coupled ADQWs 39

3.2.2 Analysis in the in-plane wavevector space 45

3.2.3 Almost-degenerate perturbation theory……………………… 47

4 Optimization of asymmetric double quantum wells……………………… 50

4.1 Enhanced QCSE in ADQWs……………………………………… 50

4.2 Optimization of ADQWs…………………………………………… 54

5 Electrooptic properties of InGaAsP-based asymmetric double quantum wells…………………………………………………………………… 59

5.1 Transmission in SQW-EAMs……………………………………… 60

5.1.1 Modeling the transmission of waveguide EAMs…………..… 60

5.1.2 Device specifications………………………………………… 61

5.1.3 Analysis in SQWs …………………………………………… 62

5.2 Enhanced slope efficiency in ADQWs…………………………….. 69

6 Conclusions…………………………………………….………………... 76

APPENDIX A……………………………………………..…….…………... 78

APPENDIX B…………………………………………………………….….... 81

REFERENCES………………………………………………………………... 82

LIST OF TABLES

Page

Table 1: Comparison of Slope Efficiencies and Other Parameters in Different QW Structures.. 75

LIST OF FIGURES

Page

Figure 1: Schematic of the applications in which optical interconnections are used…… 1

Figure 2: Optical absorption spectrum of a typical QW at (a) 70 K and (b) 300K with (red solid line) and without (black dotted) the exciton transition as a function of photon energy………………………………………………………….. 4

Figure 3: (a) Band-edge diagram of a typical single QW and the envelope functions of the quantized allowed subbands (light hole is intentionally excluded in the valence band to show clearly the symmetries of the envelopes).
(b) Absorption coefficient of a typical QW as a function of the applied electric field normal to the QW layer and the photon energy near the band-edge (the labeled narrow peaks appear as a result of excitonic transition)….. 7

Figure 4: Parameter diagram of semiconductor alloys. The four corners denoted by *B* represent the binary alloys. Along the lines of the rectangle are shown the ternary alloys denoted by *T*. Inside the rectangle is shown the quaternary alloys denoted by *Q*..……………………………………………………….. 11

Figure 5: Interpolated material parameters of $In_xGa_{1-x}As_yP_{1-y}$: (a) lattice constant of bulk, (b) strain caused by the mismatch of the lattice with the substrate when grown on InP, (c) bandgap energy of bulk, (d) bandgap energy with the existence of the strain in (b). $In_xGa_{1-x}As_yP_{1-y}$ is lattice matched along the dotted line..……………………………………………………………….. 13

Figure 6: (a) Envelope functions and (b) in-plane energy dispersions of the two lowest conduction subbands in a $GaAs/Al_{0.25}Ga_{0.75}As$..……………………. 17

Figure 7: Valence-subband dispersions along [100] direction for various well width: (a) 50 Å, (b) 100 Å, and (c) 200 Å in $GaAs/Al_{0.25}Ga_{0.75}As$ QWs..………… 19

Figure 8: (a) Envelope functions (modulus squared) and energies of the highest four valence-subbands in a 100 Å $GaAs/Al_{0.25}Ga_{0.75}As$ QW at $\mathbf{k}_{\|} = 0$ and (b) envelope functions of the four spin components of *hh1* state at $\mathbf{k}_{\|} = 25\ \mathrm{nm}^{-1}$……………………………………………………………….. 20

Figure 9: Relative motion wavefunction $\mathbf{k}_{\|}\ G_{nm}(\mathbf{k}_{\|})$ for various ground state excitons and their binding energies in a GaAs/AlGaAs SQW (well width=80 Å, Al mole fraction=0.25)..……………………………………………………….. 24

Figure 10: Exciton binding energy versus QW width in a GaAs/AlGaAs SQW (Al mole fraction=0.25)..……………………………………………………….. 24

Figure 11: In-plane wavevector dependent Overlap integrals between the first conduction subband and the major spin components of the four valence-subband in a 100 Å thick GaAs/$Al_{0.25}Ga_{0.75}As$ QW. ……………………………………………28

Figure 12: Line-broadening caused by the Fowler-Nordheim tunneling of the lowest conduction subband in InGaAsP SQWs (well width ~105 Å) for various conduction offsets as a function of the bias showing that tunneling begins to increase drastically above the direct tunneling regime………………….. 30

Figure 13: Total line-broadening of the four lowest exciton *1s*-like states as functions of electric field at room temperature in SQW-A (solid: *cb1-hh1*, dashed: *-lh1*, dotted: *-hh2*, dot-dashed: *-hh3*). Left inset: line-broadening caused by the well-width fluctuations. Right inset: measured photoluminescence linewidth in an InGaAsP QW as a function of As-mole fraction [48]……… 33

Figure 14: Energy levels and oscillator strengths of excitons in ADQW-30 as a function of the bias field strength. The inset in (a) is the band-edge diagram along the growth direction. (a) Energy levels (solid: couple excitons $E^{\alpha s,C}$, dashed: uncoupled ground-state excitons $E^{1s,UC}_{11(2)}$, dotted: band-to-band transitions $E^{d}_{11(2)}$. *e1-hh1* excitons have dots on the curves). Oscillator strengths of (b) uncoupled ground-states $f^{1s,UC}_{11(2)}$ (c) coupled ground- and excited-state excitons $f^{\alpha s,C}$ (solid) and their sum (dashed). Oscillator strengths of the coupled (d) ground- and (e) first excited-state excitons (solid) and the contributions from *e1-hh1* (dotted with marks, $f^{\alpha s,C}_{11}$) and *e1-hh2* (dotted, $f^{\alpha s,C}_{12}$) subband pairs……………………………………….. 41

Figure 15: Absorption spectra in the anticrossing bias range calculated with (right) and without (left) the inclusion of exciton mixing effects in an ADQW with BW ~ 21 Å…………………………………………………………………….. 42

Figure 16: Energy levels and oscillator strengths of excitons in ADQW-12 as a function of the bias field strength. (a) Energy levels of excitons (solids from the lowest to highest: from ground to fourth coupled excitons $E^{\alpha s,C}$, lower dashed: $E^{1s,UC}_{11}$, upper dashed: $E^{1s,UC}_{12}$). Oscillator strengths of (b) uncoupled ground-state excitons $f^{1s,UC}_{11(2)}$ (solid) and their sum (dashed) and (c) coupled excitons $f^{\alpha s,C}$ up to fourth excited states (solid), their sum (dashed: total sum, dotted: sum except $f^{1s,C}$, which shows the sequential transfer of oscillator strength to higher state). (d) and (e) are the same as those in Figure 14……………………………………………………………………. 44

Figure 17: (a) Energy dispersions of four highest valence subbands, (b) one dimensional diagonal and off-diagonal Coulomb matrix elements, (c) expansion coefficients of uncoupled ground-state excitons, (d) integrands of oscillator strengths of uncoupled ground-state excitons in Eq. (6), (e) components of coupled ground-state exciton in Eq. (8) and (f) the corresponding integrands of oscillator strengths (dotted and dashed) and their sum (solid), (g) components of coupled first excited-state exciton in Eq. (8) and (h) the corresponding integrands of oscillator strengths (dotted and dashed) and their sum (solid) as a function of the in-plane wavevector in ADQW-30 at the bias field of ~26 kV/cm. Vertical dotted line indicates the wavevector where *hh1*- and *hh2*- subbands anticross….................................... 46

Figure 18: Bias-dependent energy levels and oscillator strengths of excitons in ADQW-30 that are obtained from the almost-degenerate perturbation (ADP) theory. (a) Energy levels of excitons obtained by ADP with two bases $E_{ex}^{\alpha s,ADP}$ that show notable deviation from $E^{\alpha s,C}$. Oscillator strengths of coupled excitons (solid) from ADP with (b) two bases and (e) ten bases and their sum (dashed). Oscillator strengths of the coupled (c) ground-state and (d) first excited-state excitons from ADP with two bases (solid) and the contributions to it from *e1-hh1* (dotted with marks) and *e1-hh2* (dotted) subband pairs…... 49

Figure 19: (a) Absorption coefficient spectra of an ADQW as a function of the applied electric field and photon energy. The FWHM of the Lorentzian function is 2 meV. The anticrossing of *hh1-cb1* and *hh2-cb1* exciton is shown in the dotted circle. (b) Modulation sensitivity spectra obtained by taking the partial derivative of the absorption coefficient (a). The maximum sensitivity is observed in the dotted circle where the two lowest excitonic states anticross….. 52

Figure 20: Subband envelopes at (a) zero bias, (b) 40 kV/cm (before anticrossing), and (c) 60 kV/cm (after anticrossing)….. 53

Figure 21: Band-edge diagram of an ADQW composed of the two GaAs wells coupled through a $Al_{0.25}Ga_{0.75}As$ middle barrier and the confining walls having identical composition to the middle barrier…................................... 54

Figure 22: Maximum absorption coefficient modulation sensitivity as a function of the barrier width and FWHM (Γ) of the exciton peaks…...................... 56

Figure 23: Maximum absorption coefficient modulation sensitivity as a function of the barrier position and FWHM (Γ) of the exciton peaks…..................... 57

Figure 24: . Schematic of an InGaAsP waveguide QW-EAM [63]…..................... 61

Figure 25: Band-edge profiles of (a) SQW-A and (b) SQW-B. (Upper solid line: conduction-band edge, lower solid line: valence-band edge with only hydrostatic strain, dotted line: light hole band edge with shear strain, dashed line: heavy hole band edge with shear strain). As discussed in Section 2.1.2, the shear components of the strains in the epitaxial layers shifted the effective valence-band edges of heavy (dashed line) and light (dotted line) holes………………………………………………………………………… 63

Figure 26: Transmission loss of SQW-A in dB as a function of the applied bias voltage (solid: theory, dashed: experiment) at various wavelengths (from left to right: 1550, 1560, 1570 nm)…………………………………………… 64

Figure 27: Calculated absorption coefficients of SQW-A (a) and SQW-B (b) as functions of bias and wavelength (FWHM = 1 meV was assumed to observe the peak shift and oscillator strength clearly) and transmission loss in dB of SQW-A (c) and SQW-B (d) at room temperature [bias-dependent FWHM (e) was used for the broadening]. The horizontal dotted lines (1550 nm) meet the lowest exciton peaks at 110 (a) and 73 kV/cm (b) in SQW-A and SQW-B, respectively…………………………………………………….. 65

Figure 28: Normalized transmission curves of SQW-A (dashed) and SQW-B (solid) at various wavelengths (from left to right: 1550, 1560, 1570 nm)…………. 67

Figure 29: Transmission in dB of SQW-A (dashed) and SQW-B (solid) at various wavelength (from left to right: 1550, 1560, 1570 nm)………………………68

Figure 30: Band-edge profiles of ADQW-x where x denotes the barrier width………. 69

Figure 31: Calculated absorption coefficients (a) and transmission loss in dB (b) of ADQW-6. The cross points of vertical and dotted lines indicate where the exciton peaks were found at 1550 nm. (c) Band-edge diagrams and envelope functions at $k_{||}=0$ of the lowest electron (*cb1*) and three highest holes (solid: *hh1*, dashed:*hh2*, dotted: *lh1*) under various bias fields……………...71

Figure 32: Total line-broadening of ADQW-6 as a function of bias. The inset shows the line-broadening caused by well-width fluctuation (solid) and *cb1*-subband tunneling (dotted)………………………………………………….. 72

Figure 33: Normalized transmission curves of ADQW-6 at various wavelength (from the center: 1550, 1560, 1570 nm). Inset: transmission in dB of ADQW-6 at various wavelength (from the center: 1550, 1560, 1570 nm)………………. 73

SUMMARY

Semiconductor quantum well (QW) structures are widely adopted in optical components such lasers and photodetectors. Optical electroabsorption modulators (EAMs) that utilize QWs are known to exhibit high modulation sensitivity, which is required for the analog optical fiber link application, compared to other types of optical modulators. QW-EAMs utilize the change of absorption coefficients that depends on the change of electric field across the QW for the optical intensity modulation. This dissertation focuses on the theoretical analysis of the optical properties of asymmetric double QWs (ADQWs) and the systematic optimization of modulation sensitivity in low-voltage EAMs that incorporate ADQWs. In this structure, the accurate calculation of excitons is especially important because the excitonic as well as the band-to-band optical transitions dominate the optical properties at the operating wavelength even at room temperature. The complex linear optical susceptibility was calculated within the density matrix approach in the quasi-equilibrium regime for the low excitation power and through a thorough treatment of line broadening, which is required for the calculation of the transmission properties of the QW-EAMs. Transition strengths were calculated in the wavevector space, which effectively includes valence subband mixing with the warping of the subbands, excitonic mixing effects, and possible optical selection rules (*e.g.*, light polarization, spin of excitons). The calculated transmission properties were almost identical to the experimental data at the device operating bias range. The mixing of excitons in ADQWs was analyzed in detail in momentum space, which was demonstrated to be very important in the process of structural optimization of ADQWs. The

optimization of the structural parameters revealed that at an adequate barrier position and well width, the barrier thickness affects the modulation efficiency the most. Subsequently, in InGaAsP-based waveguide type QW-EAMs that operate at 1550 nm, the optimization of only one variable—the thickness of the coupling barrier—of the ADQWs shows 380 % enhancement in the modulation sensitivity at a much lower bias field (70 → 35 kV/cm) compared with that of single-QW structures. This enhancement is found to be caused by the strong mixing of the two exciton states originating in different subband pairs.

CHAPTER 1

INTRODUCTION

Optical interconnections are currently widely used and will expand in the future the application areas where the conventional metal-wired electrical or wireless electromagnetic data transmission is not feasible due to high data rates, high signal losses, interferences, couplings, long interconnection distances, etc. Some of the applications, *e.g.*, between chips on a board, between boards in a workstation, from the base station to the remote antenna (or radio-over-fiber) or to the home, and between hub-stations are depicted in Figure 1. Depending on the applications, the interconnection distance ranges from a few cm (chip to chip) to over several hundred km (hub to hub), and the data to

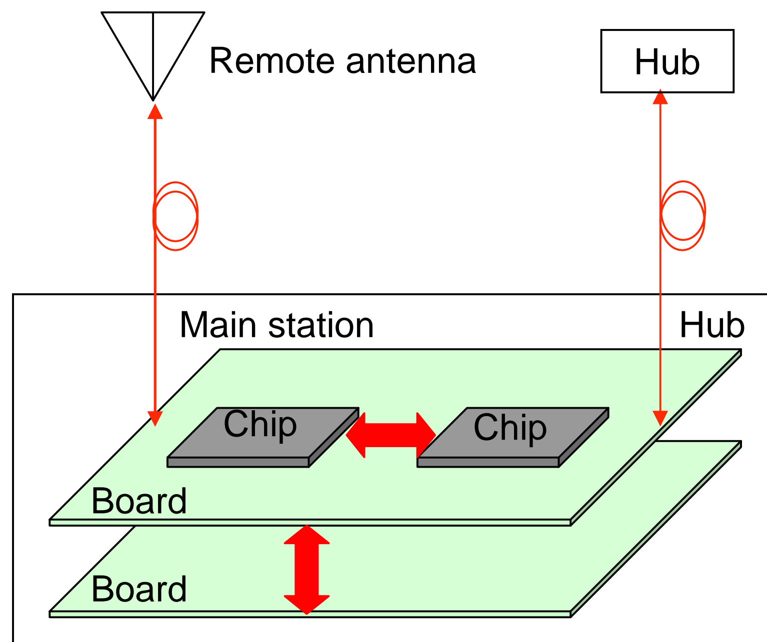

Figure 1. Schematic of the applications in which optical interconnections are used.

be transmitted can be either analog or digital. Typical optical communication systems are basically composed of three functional units: transmitter, channel, and receiver. The transmitter modulates *light*, the carrier, to convey the data. There are several light modulation schemes, including intensity, frequency, phase, and polarization modulations. Among them, intensity modulation is the most widely used due to the simplicity of the demodulation to an electrical signal using a photodetector [1] at the receiver unit. Intensity modulation can be realized either by directly modulating the light output of the laser or by modulating the constant laser output using an external optical modulator. The latter has several advantages over the former such as higher modulation speed, higher modulation sensitivity (or efficiency), and low parasitics. These, in fact, make external modulation especially suitable for analog data applications, which is the main focus of this study.

Two types of external optical intensity modulators are widely used: electrooptic modulators and electroabsorption modulators (EAMs). Electrooptic modulators are realized by Mach-Zehnder interferometers using $LiNbO_3$ or bulk semiconductors, which exhibit highly electric-field-dependent refractive index. These operate stably at fairly high input optical power due to low absorption coefficients. To obtain the required fundamental performance of the modulator, *i.e.*, the modulation efficiency, however, the size of the device (or the interaction length of the light with the material) should be very large (> a few cm), which also increases the cost of the device. EAMs, on the other hand, use the change of absorption coefficient of bulk semiconductors or semiconductor heterojunction quantum wells (QWs). Since the required interaction length is typically very short, the EAMs can be made very small (<1 mm, in principle) and inexpensive.

Furthermore, they can be integrated with other semiconductor optical devices such as lasers [2]. Compared to bulk semiconductors which utilize only the intrinsic properties that are determined by the materials, QWs have more degrees of freedom in designing the devices for the required performance due to bandgap engineering.

A unique feature of the optical properties of the QWs is that the exciton transitions are greatly enhanced due to the confinement of the carriers inside the QWs. An exciton is a hydrogen-like quasi-particle consisting of a bound state of an electron and a hole by the Coulomb force. The optical exciton transitions occur slightly below the band-to-band transition edge separated by the binding energy of the exciton. Compared to values in bulk semiconductors, the binding energies of excitons in QWs are typically much larger (4 times that of bulk in an ideal two-dimensional case) yielding higher oscillator strengths [3]. As shown in Figure 2(a), the exciton absorption peak is clearly observable at low temperature right below the edge of band-to-band transitions. As the temperature increases, the excitonic peak broadens due to scattering with phonons and, depending on the materials and geometries of the QWs, the excitonic peak may or may not be observable. Even in the latter case where the broadening is significant and consequently the peak is considerably broadened, however, we should expect that the total absorption strength nonetheless is derived from both the band-to-band and the excitonic transitions, as depicted in Figure 2(b). Considering the facts that most of the QW-EAMs operate quite below the band-edge of the QWs to reduce the insertion loss and that the band-edge optical properties of QWs are strongly dependent on the exciton transition, one can infer that accurate analysis of excitons and band-to-band transitions is very important in the estimate of the performance of QW-EAMs.

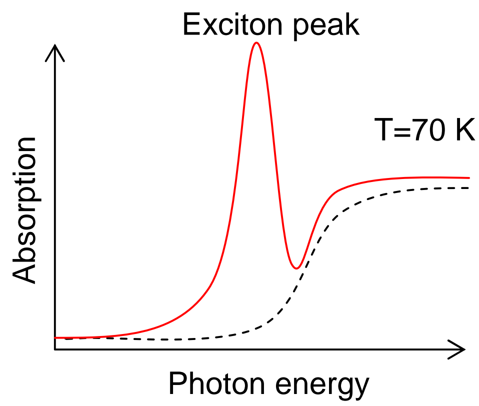

(a)

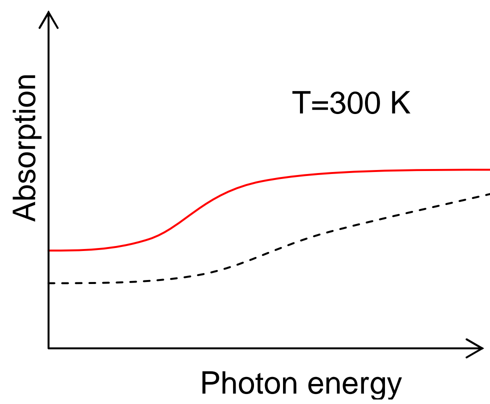

(b)

Figure 2. Optical absorption spectrum of a typical QW at (a) 70 K and (b) 300K with (red solid line) and without (black dotted) the exciton transition as a function of photon energy.

There has been much effort to model theoretically the excitonic absorption properties of QWs since the first experimental observation of excitonic peaks in a QW in 1974 [4]. The basic theories of excitonic optical absorption in bulk semiconductors and in perfect two-dimensional (2D) structures were fairly well established in 1957 [5] and 1966 [3], respectively. In Ref. [3], the bound and unbound excitonic states were modeled in a perfect 2D structure as 2D hydrogen using the effective-mass and envelope-function approximations and the polarization-dependent optical absorption intensities of the states were derived. The quasi-2D excitonic states were calculated using the variational method that included the dependence of QW width in the early 1980s [6]-[8], which resulted in good agreements with the experimental data. The inclusion of differences in the effective mass [9] and the dielectric constant [10] between the barrier and well materials and the effect of valence-band mixing (VBM) [11] increased the accuracy of results of the calculation. Later, a momentum-space approach [12]-[14] has been found to be very convenient to obtain accurately fine structures of the excitons while including VBM, although it requires intense numerical calculation.

When an electric field is applied perpendicular to the QW layers, the allowed energies of the subbands that are quantized along the confined direction shift down to lower energy while keeping most of the envelope function inside the QW, which, in terms of the optical properties, eventually decreases the optical transition energy between the associated conduction and valence subbands while keeping substantial oscillator strength. This electroabsorption effect in QWs, called the quantum-confined Stark effect (QCSE) [15], is the fundamental operating principle of QW-EAMs. This is not expected in bulk semiconductors [16] or in a QW with a field applied parallel to the QW layer,

[17] where the excitons are easily dissociated by relatively weak electric fields, and is strongly dependent on the potential structures of the QWs. In Figure 3 are presented the quantized subbands and their envelope functions in a typical single QW and its field-dependent absorption spectra at low temperature in a range of photon energy near the band-edge, which clearly shows the Stark shift of the lowest excitonic absorption peak [labeled *hh1-cb1* in Figure 3(b)] as the electric field increases.

Theoretical and experimental investigations of the QCSE were initiated in the early 1980s [15],[18],[19]. When the QCSE was first demonstrated experimentally, optical EAMs were immediately identified as an application [19]. The fabricated structure was a multiple QW (MQW), whose performance as an optical modulator was actually quite poor. Later on, there was considerable effort to enhance the QCSE by changing the geometry of the QW. Studies on symmetrically coupled DQWs showed that the change in oscillator strength and Stark shift were enhanced compared with those of single QWs (SQWs) [20]-[24]. Asymmetric coupled DQWs (ADQWs) revealed much more drastic changes in electric-field-dependent absorption coefficients and refractive indices [25]-[29] due to the breaking of inversion symmetry (leading to a first-order QCSE). These studies explored in essence the physics of coupled DQWs such as level anticrossing (see Figure 19 in Chapter 4) and the corresponding mixing of excitons, which is the main reason for the enhancement of QCSE, however only fractionally, *i.e.,* in a fixed electric field or by using simple exciton models.

Despite the proven enhancement of QCSE in ADQWs [25]-[29], only SQWs have been adopted for the applications to QW-EAMs until recently [30],[31], presumably due to the relative complexity of the fabrication processes and the lack of a through physical

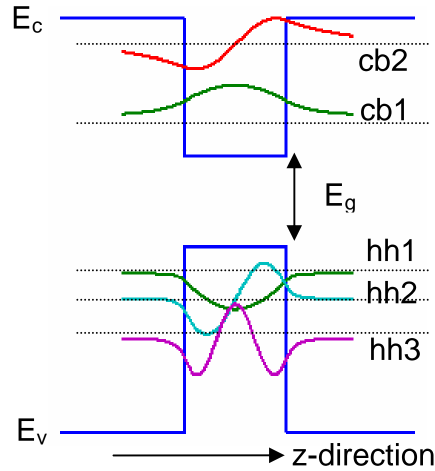

(a)

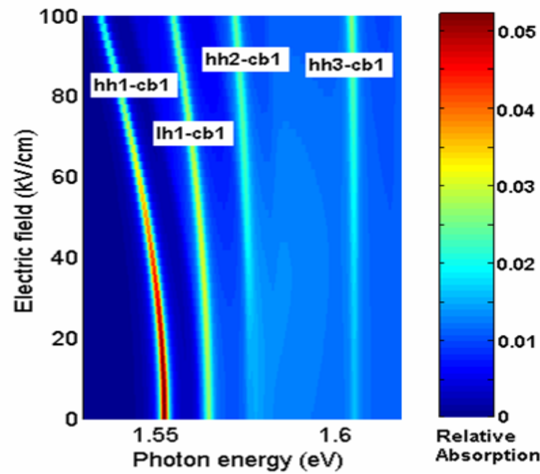

(b)

Figure 3. (a) Band-edge diagram of a typical single QW and the envelope functions of the quantized allowed subbands (light hole is intentionally excluded in the valence band to show clearly the symmetries of the envelopes). (b) Absorption coefficient of a typical QW as a function of the applied electric field normal to the QW layer and the photon energy near the band-edge (the labeled narrow peaks appear as a result of excitonic transition).

understanding of and optimization of the ADQWs. In this dissertation, we analyze theoretically the optical properties of QWs, explore the physics of mixing of excitons and their oscillator strengths in the anticrossing bias range in ADQWs [32], and optimize the band-edge profile of ADQWs to exhibit maximum modulation efficiencies. The complex optical susceptibility which governs the interaction of lights with the QWs is obtained by the standard perturbative expression in the optical field [33]. The exciton and valence-to-conduction subband-to-subband transitions are included in the calculation. The momentum space approach was used in calculating the excitons to take into account both VBM and mixing of the excitons. Also, detailed considerations are taken into in interpolating the material parameters of compound semiconductors [34],[35] and the line-broadening of the optical transitions [36]. The fundamental theories required for the calculation are discussed in Chapter 2. In Chapter 3, the physics of the mixing of excitons in the anticrossing bias range in ADQWs is presented in detail in addition to the limitations of the simplified exciton models. The dependence of the modulation sensitivity ($d\alpha/dE$, change in optical absorption coefficient per change in electric field across the QW) on several structural parameters of ADQWs including the width and position of the middle coupling barrier and the overall well width is analyzed in Chapter 4 [37]. In Chapter 5, we pick a recently reported waveguide-type InP-based QW-EAM which operates at 1550 nm and compare the experimental bias-dependent transmission data with our simulation results. Further, we extend our analysis to ADQWs to obtain considerable enhancement of the performance of QW-EAMs [38].

CHAPTER 2

LINEAR OPTICAL PROPERTIES OF QUANTUM WELLS

The propagation of light in media can be described fully by Maxwell's equation in a classical electromagnetic theory using the known optical properties of the media within the relevant frequency band. When the power of the light is sufficiently low (*i.e.*, low excitation regime), the optical properties of the semiconductor QWs can be described by its linear optical susceptibility, which can be calculated theoretically as we discuss in this chapter. In this limit, the frequency-dependent absorption coefficient $\alpha(\omega) \approx (4\pi\omega / n_b c) \cdot \chi''(\omega)$ and the refractive index $n(\omega) \approx \sqrt{1 + 4\pi\chi'(\omega)}$ of the medium are obtained from $\chi(\omega) = \chi'(\omega) + i\chi''(\omega)$, where χ' and χ'' are the real and the imaginary parts of the linear complex optical susceptibility χ, n_b is the background refractive index, and c is the speed of light. Since most QW-EAMs operate right below the band-gap frequency of the QWs to reduce the insertion loss, we limit our range of analysis around the band-edge of the QWs where the optical interband and excitonic transitions dominate the susceptibility.

The following shows the sequential procedure of calculating the susceptibility of a QW in a given range of the optical wavelength:

(1) Interpolate the material parameters of the compound semiconductor alloys from those of the known binary alloys and define the band structure of the QW.

(2) Calculate the electronic properties *i.e.*, subband structures.

(3) Calculate the exciton states.

(4) Calculate the optical matrix elements between subbands.

(5) Calculate the oscillator strengths of excitons.

(6) Estimate the line broadening of the allowed optical transitions.

(7) Obtain the susceptibility by adding the subband-to-subband and excitonic transitions.

The result of each step is required for the calculation of the following step. To obtain the electric-field-dependent susceptibility, all of the above procedures need to be repeated from step (1) by modifying the band structure for each new value of the electric field, which is the adiabatic approach valid in the low modulation frequency [39].

2.1 Material parameters of alloys and band-edge profiles

The quantum heterostructures are realized by subsequently growing semiconductor alloys that have different bandgaps, typically by means of molecular beam epitaxy (MBE) or metal-organic chemical vapor deposition (MOCVD). The band-edge profiles that are required to calculate the allowed electronics states in the quantum structures can be obtained from the band parameters of each alloy. Accurate material parameters of the semiconductor alloys are thus crucial to obtain valid results. Since the complete experimental parameter maps for ternary or quaternary alloys are not always available, one has to resort to plausibly interpolated data from those of the known binaries (*e.g.*, parameters for $In_xGa_{1-x}As_yP_{1-y}$ can be obtained from those of InP, InAs, GaP, and GaAs). In this section, we discuss how to obtain the required material parameters of the alloys and draw the band-edge diagram.

2.1.1 Material parameters of alloys

The parameter diagram of semiconductor alloys is shown in Figure 4. *B*, *T*, and *Q* denote binary, ternary, and quaternary material parameters, respectively.

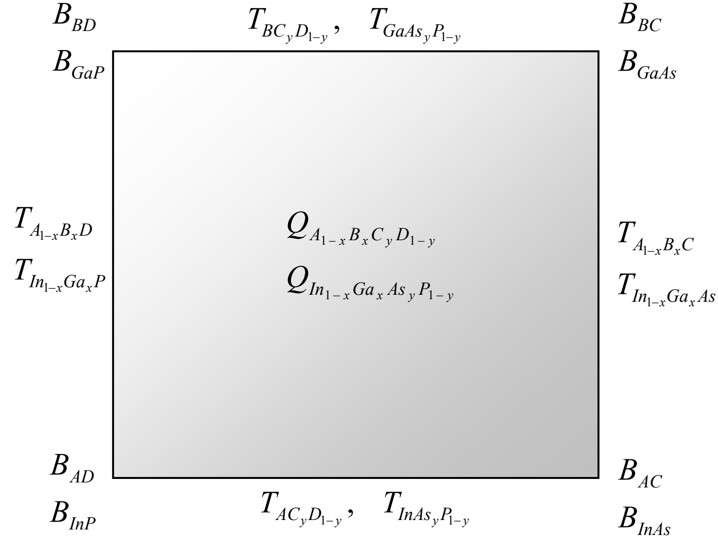

Figure 4. Parameter diagram of semiconductor alloys. The four corners denoted by *B* represent the binary alloys. Along the lines of the rectangle are shown the ternary alloys denoted by *T*. Inside the rectangle is shown the quaternary alloys denoted by *Q*.

Material parameters of a ternary alloy $T_{A_xB_{1-x}C}$ that is composed of the atomic elements *A*, *B*, and *C* can be obtained from the known parameters of binary materials B_{AC} and B_{BC} using the quadratic interpolation:

$$T_{A_xB_{1-x}C} = (1-x)B_{BC} + xB_{AC} - x(1-x)BP_{ABC}\,, \tag{1}$$

where BP_{ABC} is the quadratic bowing parameter that is obtained experimentally. When the bowing parameter *BP* is set to zero, Eq. (1) reduces to the linear interpolation. Binary parameters and bowing parameters of major compound semiconductors are thoroughly reviewed by Vurgaftman *et al.* [35].

The quadratic interpolation equation (1) for ternaries can be extended to obtain the parameters of quaternaries. Except for the bandgap energy, we use the following equation by Glisson [40] to obtain the parameters of the quaternaries:

$$Q_{ABCD}(x,y)=\frac{x(1-x)[(1-y)T_{ABD}(x)+yT_{ABC}(x)]+y(1-y)[xT_{BCD}(y)+(1-x)T_{ACD}(y)]}{x(1-x)+y(1-y)}. \quad (2)$$

Here Q and T are the quadratically interpolated material parameter of the ternaries and quaternaries, respectively. For the bandgap energies E_g, however, we adopt the recently developed biquadratic interpolation scheme [34],

$$\begin{aligned} Q_{ABCD}(x,y) &= (1-x)[(1-y)B_{AD}+yB_{BD}]+x[(1-y)B_{BD}+yB_{BC}] \\ &-x(1-x)[(1-y)BP_{ABD}+yBP_{ABC}]-y(1-y)[(1-x)BP_{ACD}+xBP_{BCD}] \\ &+x(1-x)y(1-y)D, \end{aligned} \quad (3)$$

where D is the biquadratic bowing parameters for quaternary alloys. When the bowing parameters BPs and D are set to zero, Eq. (3) reduces to a bilinear interpolation. When only D is zero, Eq. (3) is equivalent to the quadratic interpolation developed previously by Moon *et al.* [41]. The biquadratic bowing parameter D is currently available only for the bandgap energy in Ref. [34].

For the electron effective mass m_e^*, instead of the direct interpolation from those of the binary alloys, Vurgaftman *et al.* suggests the following in which the parameters on the right-hand side are the interpolated values using Eqs. (2) and (3),

$$\frac{m_0}{m_e^*}=(1+2F_K)+\frac{E_P(E_g+2\Delta_{SO}/3)}{E_g(E_g+\Delta_{SO})}, \quad (4)$$

where m_0 is the free electron mass, F_K is the Kane parameter, E_P is the interband matrix element, E_g is the bandgap energy, and Δ_{SO} is the spin-orbit splitting.

Figure 5 shows examples of the material parameters of $In_xGa_{1-x}As_yP_{1-y}$ that is epitaxially grown on InP substrate. Other parameters can also be drawn exactly the same way.

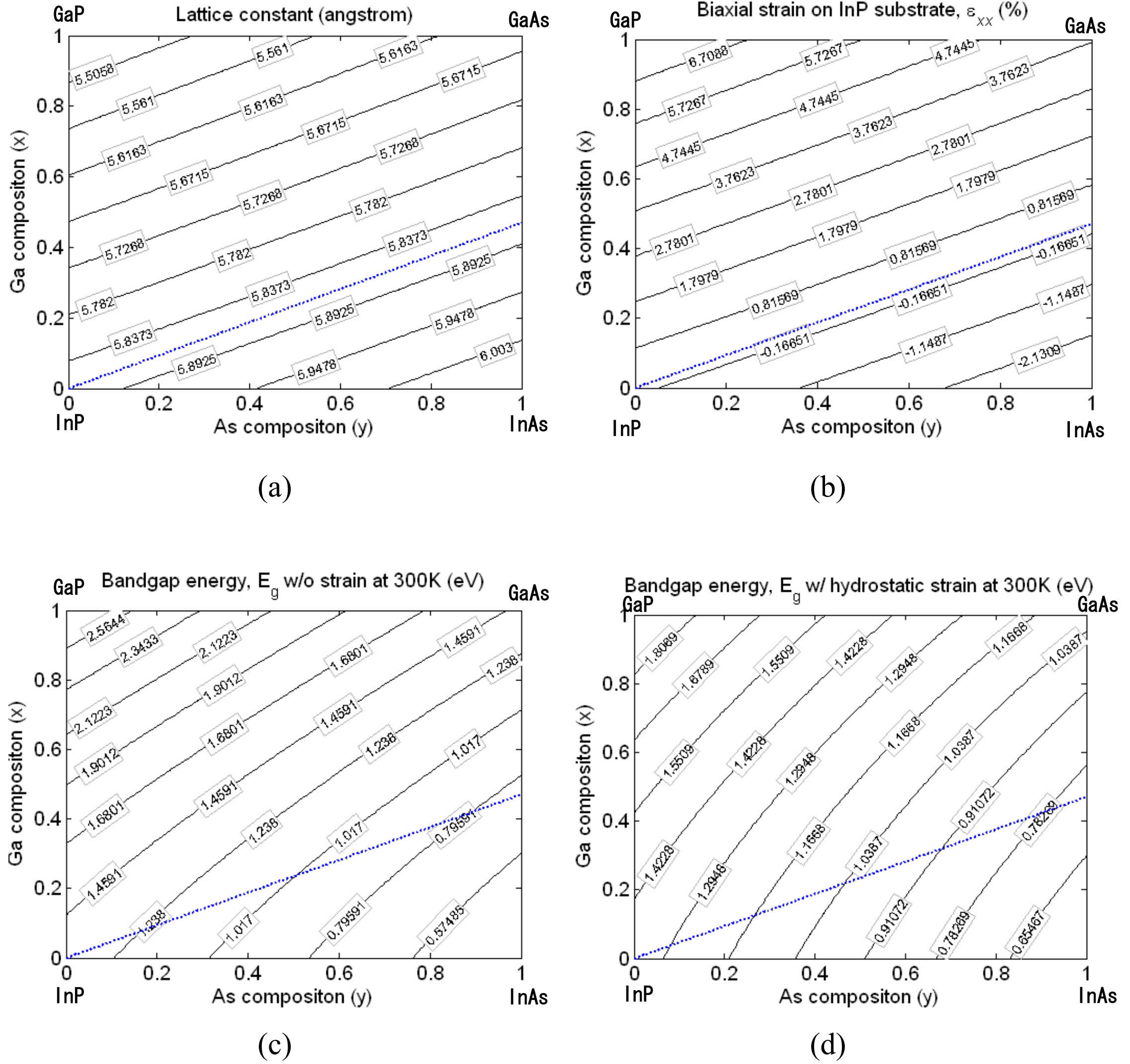

Figure 5. Interpolated material parameters of $In_xGa_{1-x}As_yP_{1-y}$: (a) lattice constant of bulk, (b) strain caused by the mismatch of the lattice with the substrate when grown on InP, (c) bandgap energy of bulk, (d) bandgap energy with the existence of the strain in (b). $In_xGa_{1-x}As_yP_{1-y}$ is lattice matched along the dotted line.

2.1.2 Band-edge profiles

The band-edge line-up at the junction of two layers can be obtained using $\Delta E_{c,12} = E_{g,1} - (\Delta E_{v,12} + E_{g,2})$, where $\Delta E_{c,12}$ and $\Delta E_{v,12}$ are conduction- and valence-band offsets between layer 1 and 2, respectively and $E_{g,i}$ is the bandgap energy of the layer-*i*. The valence-band offset of quaternary layer-*i* referenced to the valence-band edge of the InP substrate $\Delta E_{v,i-InP}$ can be obtained by the linear interpolation of those of binary alloys.

The deformation of the band edge of a layer must be included when the strain induced by lattice mismatch with the substrate exists [42]. For example, in InGaAsP heterostructures, unless the compositions are chosen along the dotted line in Figure 5, strain will be present. The hydrostatic component of the strain deforms both the conduction- and valence-band edges changing the bandgap energy of the layer, which simultaneously changes m_e^* according to Eq. (4), while the shear component acts only on the valence band-edge with equal magnitude, but with opposite signs, on the heavy- and light-hole bands.

2.2 Subbands in quantum wells

We use the envelope-function approximation for the calculation of the subband states in the QWs within the effective-mass theory. The electronic subband states are calculated variationally by treating them as quasi-bound in an effective confinement region [43]. The conduction subbands are calculated by assuming a constant effective electron mass. The valence subbands are, however, obtained by using the Luttinger-Kohn Hamiltonian since this allows us to include the valence-subband nonparabolicity and

wavevector-dependent overlap integral between subbands that are involved in the optical transitions, which is known to be important for accurate exciton calculations.

2.2.1 Conduction subbands

The conduction subband state in a QW with confinement potential $V(z_e)$ along the growth direction is expressed as

$$\left|\mathbf{k}_{\|}, n\right\rangle = f_n(z_e, \mathbf{k}_{\|}) e^{i\mathbf{k}_{\|}\cdot\boldsymbol{\rho}_e} U^c(\mathbf{r}), \tag{5}$$

where $\mathbf{k}_{\|}$ is the in-plane wavevector, n is the subband index, $f_n(z_e, \mathbf{k}_{\|})$ is the slow-varying envelope function, $\boldsymbol{\rho}_e=(\rho_e,\theta)$ is the in-plane position vector, and $U^c(\mathbf{r})$ is the fast-varying conduction-band Bloch function. Because the electrons move freely along the plane of the QW, the in-plane wavefunction is expressed as the exponential term in Eq. (5). The Hamiltonian for the conduction subbands in the effective mass approximation is

$$H_e = \frac{p_{\|}^2}{2m_e^*} + \frac{p_z^2}{2m_e^*} + V_e(z), \tag{6}$$

where $p_{\|}$ and p_z are the in-plane and the growth-direction momentum operators, respectively. Due to the confinement, the allowed states and energies are quantized along the z-direction in the QWs. The kinetic energy of the 2D in-plane motion, however, is that of the free particle that has the effective mass and the $k_{\|}$-dependent energy of the electron follows the quadratic behavior in each subband.

The energy dispersion relations and envelope-functions of the conduction-(valence-) subbands can be conveniently calculated variationally [44] for arbitrary shaped QW structures. Gaussian type functions ($\left|l,\beta\right\rangle = z^l e^{-(\beta z)^2}$, $l = 0,1$ with β chosen large

enough to ensure accurate envelope-functions and numerical stability) are usually used for the (non-orthogonal) basis-function set. The number of the basis function can be increased until the resulting allowed energies converge sufficiently. By expanding the envelope-function as a linear combination of the basis-functions, the Schrödinger equation becomes a generalized eigenvalue problem: $H\Psi = SE\Psi$, where H is the Hamiltonian matrix, S is the overlap integral matrix of the basis set, and E is an eigenvalue of energy.

Figure 6 shows the calculated envelope functions and energy dispersions of the two lowest conduction subbands in a typical GaAs/AlGaAs single QW. Because of the fixed electron effective mass, the energy dispersions are quadratic [Figure 6(b)] and the envelope functions do not change from those at $k_{\|} = 0$ as shown in Figure 6(a).

2.2.2 Valence subbands

In the valence band, the confined state of a particle can be obtained using the Luttinger-Kohn Hamiltonian of the bulk crystal and considering the confinement potential $V_h(z)$. The detailed derivation of the Luttinger-Kohn Hamiltonian for the bulk crystal can be found in standard solid-state physics textbooks [45]. Here, we adopt the 4×4 Hamiltonian matrix, which excludes the split-off band (detailed expression is shown Eq. (A1-1) in Appendix A). The split-off band need not be considered for QWs with moderate potential depth (a few hundred meV) because the energy extremum of the split-off band is separated far enough from the heavy- and light-hole bands and typically interacts only weakly with the heavy- and light-hole bands. The valence-subband structure of a QW can be obtained by including the valence-band potential $V_h(z)$ in the diagonal entries of the Hamiltonian matrix and replacing the *z*-component wavevector k_z

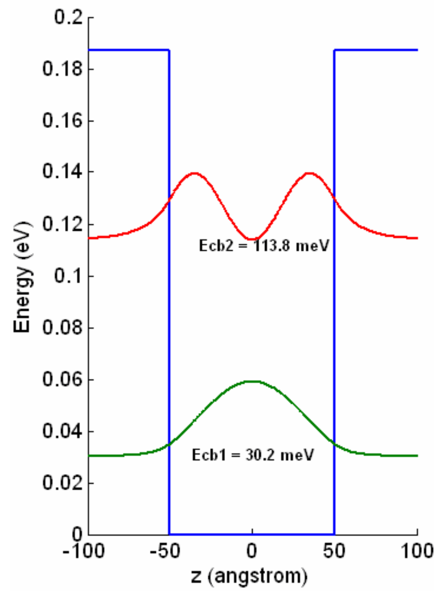

(a)

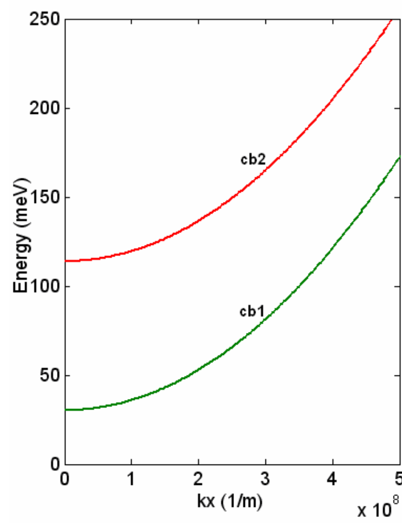

(b)

Figure 6. (a) Envelope functions and (b) in-plane energy dispersions of the two lowest conduction subbands in a $GaAs/Al_{0.25}Ga_{0.75}As$.

by the momentum operator $-i\partial/\partial z$. We assume that the Bloch functions in the well and barrier materials are the same, which is valid for typical cubic semiconductors. In the envelope-function approximation, the wavefunction of the valence subband is written as

$$\left|\mathbf{k}_{\|}, m\right\rangle = \sum_{\nu} g_m^{\nu}(z_h, \mathbf{k}_{\|}) e^{i\mathbf{k}_{\|}\cdot\boldsymbol{\rho}_h} U^{\nu}(\mathbf{r}), \quad (7)$$

where m is the valence-subband index, $g_m^{\nu}(z_h, \mathbf{k}_{\|})$ is the in-plane wavevector $\mathbf{k}_{\|}$-dependent z-component of the envelope-function with the spin component ν=±1/2 or ±3/2, and $U^{\nu}(\mathbf{r})$ is the bulk valence-band Bloch function at the center of the Brillouin zone. When $\mathbf{k}_{\|} = 0$, the off-diagonal elements of the Hamiltonian are zeros and the resulting subband states are not combinations of the four states in Eq. (7) but have only one component in the summation, *i.e.*, not a mixed state. When $\mathbf{k}_{\|} \neq 0$, however, the off-diagonal elements in the Hamiltonian have nonzero values and the corresponding subbands are the mixed states of the four components in Eq. (7). Figure 7 shows the calculated energy dispersion of valence-subbands along [100] direction for GaAs/$Al_{0.25}Ga_{0.75}As$ SQWs. These results are in excellent agreement with those obtained by numerous other groups (*e.g.*, Ref. [11] and Refs. therein). The energy separation between subbands is larger in a narrower QW. The dispersion curves deviate markedly from parabolic and due to hybridization of heavy- and light-hole states, which results from nonzero off-diagonal Hamiltonian elements when $\mathbf{k}_{\|} \neq 0$. Figure 8 shows the squared modulus of the valence subband envelope-functions of *hh1*-state along the z-direction at $\mathbf{k}_{\|} = 0$ and $\mathbf{k}_{\|} = 25\,\text{nm}^{-1}$ in a 100 Å wide GaAs/$Al_{0.25}Ga_{0.75}As$ SQW. The subband energies in the figure are measured with respect to the bulk valence-band edge.

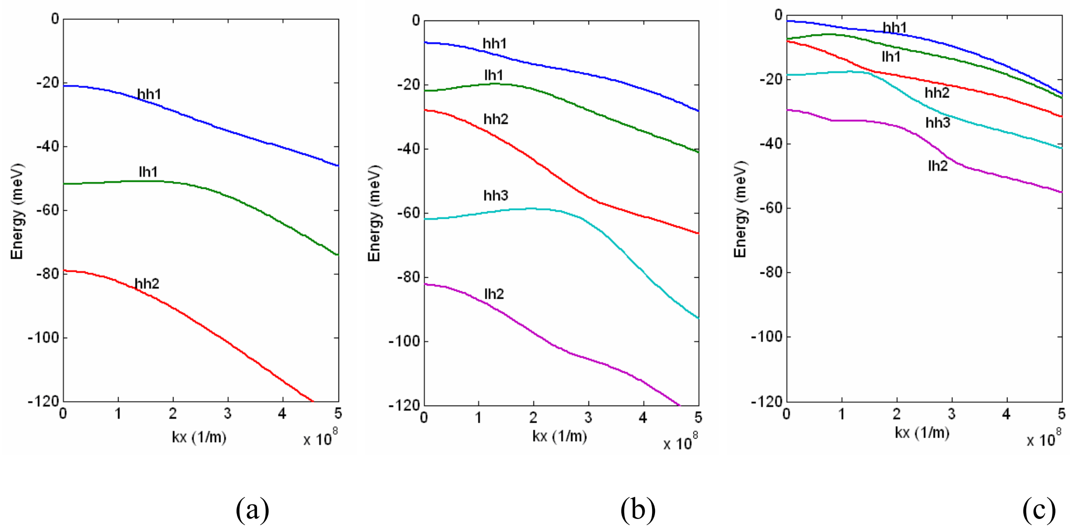

(a) (b) (c)

Figure 7. Valence-subband dispersions along [100] direction for various well width: (a) 50 Å, (b) 100 Å, and (c) 200 Å in GaAs/$Al_{0.25}Ga_{0.75}As$ QWs.

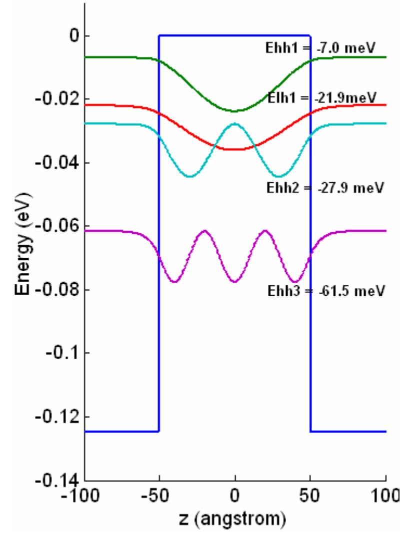

(a)

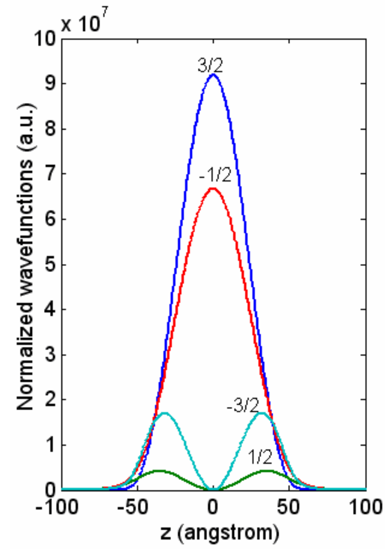

(b)

Figure 8. (a) Envelope functions (modulus squared) and energies of the highest four valence-subbands in a 100 Å GaAs/$Al_{0.25}Ga_{0.75}As$ QW at $\mathbf{k}_{\parallel} = 0$ and (b) envelope functions of the four spin components of *hh1* state at $\mathbf{k}_{\parallel} = 25\,\mathrm{nm}^{-1}$.

2.3 Excitons in quantum wells

The attractive Coulomb interaction between an electron in a conduction-subband and a hole in a valence-subband results in a hydrogen-like quasi-particle called an exciton. These include discrete bound states that play a central rôle in the optical properties of interest here. We calculate the QW exciton states in momentum space to include more easily valence subband mixing and the excitonic mixing effect. The detailed excitonic theory adopted here can be found in Refs. [12]-[14]. In this section, we outline the fundamentals of the theory.

Within the framework of effective-mass theory, the exciton envelope function in a quasi-2D structure is expressed as a linear combination of the associated electron and hole eigenstates,

$$\Psi_{\alpha,env} = \sum_{n,m} \sum_{\mathbf{k}_{\|},\mathbf{q}_{\|}} F^{\alpha}_{nm}\left(\mathbf{k}_{\|},\mathbf{q}_{\|}\right) \cdot e^{i(\mathbf{k}_{\|}\cdot\boldsymbol{\rho}_e+\mathbf{q}_{\|}\cdot\boldsymbol{\rho}_h)} f_n(z_e,\mathbf{k}_{\|}) \sum_{\nu} g^{\nu}_m(z_h,\mathbf{q}_{\|}) , \tag{8}$$

where α is an index that labels the exciton states and $F^{\alpha}_{nm}\left(\mathbf{k}_{\|},\mathbf{q}_{\|}\right)$ are the expansion coefficients that represent the contribution of the subband pairs at the given wavevectors to the exciton state. The envelope function $\Psi_{\alpha,env}$ is an eigenfunction of the exciton Hamiltonian

$$H_{ex} = \frac{\mathbf{p}_e^2}{2m_e} + V_e(z_e) + H_{LK} + V_h(z_h) - \frac{e^2}{\varepsilon\left|\mathbf{r}_e - \mathbf{r}_h\right|} \tag{9}$$

where $V_{e(h)}$ is the band-edge profile of the conduction (valence) band, H_{LK} is the 4×4 Luttinger-Kohn Hamiltonian for the hole, and the last term is the Coulomb interaction between the electron and the hole that are located at $\mathbf{r}_e$ and $\mathbf{r}_h$, respectively.

The equation for the expansion coefficients is obtained by multiplying the Schrödinger equation $H_{ex}\Psi_{\alpha,env}=E_{\alpha}\Psi_{\alpha,env}$ with the electron and hole envelope functions on

the left followed by an integration in real space. In doing so, we assume that light interacts with excitons at rest (*i.e.,* the photon momentum is negligible) so that $F_{nm}^{\alpha}(\mathbf{k}_{\|},\mathbf{q}_{\|}) = \delta(\mathbf{k}_{\|}+\mathbf{q}_{\|})G_{nm}^{\alpha}(\mathbf{k}_{\|})$ and we further apply the axial approximation to the hole state so that $g_{m}^{\nu}(z_h,\mathbf{k}_{\|}) = g_{m}^{\nu}(z_h,k_{\|})e^{-i\nu\varphi}$. The physical basis of the former is that the photon momentum is negligible on the scale in momentum space over which the excitonic states vary with center-of-mass momentum; that of the later is that warping effectively averages out in the determination of the excitonic states. We also express the expansion coefficient $G_{nm}^{\alpha}(\mathbf{k}_{\|})$ in terms of its magnitude and phase as $G_{nm}^{l\alpha}(k_{\|})e^{il\varphi}$ (axial approximation decouples the excitons that have different *l*-values [8]). The resulting equation for $G_{nm}^{\alpha}(\mathbf{k}_{\|})$ becomes independent of the angle φ

$$\left[E_n^e(k_{\|}) - E_m^h(k_{\|})\right]G_{nm}^{l\alpha}(k_{\|}) + \sum_{n',m'}\sum_{\mathbf{k}'_{\|}} V_{nm,n'm'}^{l}(\mathbf{k}_{\|},\mathbf{k}'_{\|})G_{n'm'}^{l\alpha}(k'_{\|}) = E_{l\alpha}G_{nm}^{l\alpha}(k_{\|}) \tag{10}$$

except for the Coulomb interaction $V_{nm,n'm'}^{l}$

$$\begin{aligned} &V_{nm,n'm'}^{l}(k_{\|},k'_{\|},\varphi') \\ &= \frac{-e^2}{\varepsilon q}\iint dz_e dz_h f_{n'}^{*}(z_e) f_n(z_e) \sum_{\nu} g_{m'}^{\nu\,*}(k'_{\|},z_h) g_m^{\nu}(k_{\|},z_h) e^{-q|z_e - z_h|} e^{i(l-\nu)\varphi'} \end{aligned} \tag{11}$$

where $q = \sqrt{k_{\|}^{2} + k'^{2}_{\|} - 2k_{\|}k'_{\|}\cos\varphi'}$, φ' is the angle between $\mathbf{k}_{\|}$ and $\mathbf{k}'_{\|}$, $E_n^e(k_{\|}) - E_m^h(k_{\|})$ is the joint energy dispersion of the *n*-th electron and *m*-th hole subbands, and $E_{l\alpha}$ is the eigenenergy of the $l\alpha$-th state. The singularity arising along $k_{\|}=k'_{\|}$ in the denominator q of Eq. (11) in the numerical analysis is eliminated by accounting for screening induced by intrinsic carriers [46]. The envelope function for the exciton now becomes

$$\Psi_{\alpha,env}^{l} = \sum_{n,m}\sum_{k_{\|}} G_{nm}^{l\alpha}(k_{\|}) f_n(z_e) \sum_{\nu} e^{i(l-\nu)(\theta-\pi/2)} g_m^{\nu}(z_h,k_{\|}) J_{l-\nu}(k_{\|}\rho) \tag{12}$$

where J_{l-v} is the $(l-v)$-th order Bessel function and ρ and θ are the magnitude and angle of the relative position vector $(\boldsymbol{\rho}_e - \boldsymbol{\rho}_h)$ of the exciton. In Eq. (12), the l-th exciton state is the sum of four spinor components of the valence subbands and $(l-v)$ in the exponential term is the orbital angular momentum of the exciton component v. In the limit of the two-band model (one conduction- and one valence-subband states) and by assuming that the valence subbands do not mix strongly, we can safely define the 2D orbital angular momentum quantum number of the l-th exciton state as $m_l = l - v_m$ (analogous to the H-atom: $m_l = 0$, ± 1, ± 2 … for s-, p-, d-like … state, respectively) because the state is dominated by one of the four contributing component v_m. For instance, the *e1-hh1* exciton in an unbiased fairly narrow SQW is dominated by $v_m = \pm 3/2$ [for spin up (+) and down (–)] and $l = v_m$ and $l = v_m \pm 1$ for s-like ($m_l = 0$) states and p-like ($m_l = \pm 1$) states, respectively. The variational approach is a convenient tool of solving Eq. (10), which is carried out by expanding $G_{nm}^{l\alpha}(k_{\parallel})$ in a truncated set of Gaussian basis functions that minimizes the eigenenergy [8].

Figure 9 shows the expansion coefficients $G_{nm}^{l\alpha}(k_{\parallel})$ of the exciton ground state multiplied by the in-plane wavevector and their binding energies calculated within the two-subband model in a typical GaAs/AlGaAs SQW (compare with the results in Ref. [47]). The dependence of the exciton binding energy on the well-width is plotted in Figure 10. In the region where the well-width exceeds 100 Å, the binding energies decrease as the well-width increases, which is due to the increase of the penetration of subband wavefunctions into the barriers. While for very small well-width, the binding energies also decrease for the same reason, which is well observed on the *hh3-cb1* exciton curve in Figure 10.

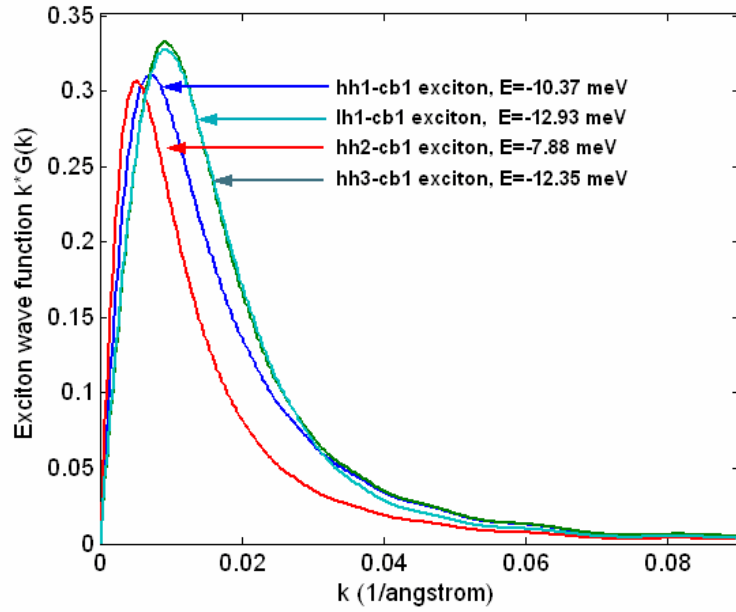

Figure 9. Relative motion wavefunction $\mathbf{k}_{\|}G_{nm}(\mathbf{k}_{\|})$ for various ground state excitons and their binding energies in a GaAs/AlGaAs SQW (well width=80 Å, Al mole fraction=0.25).

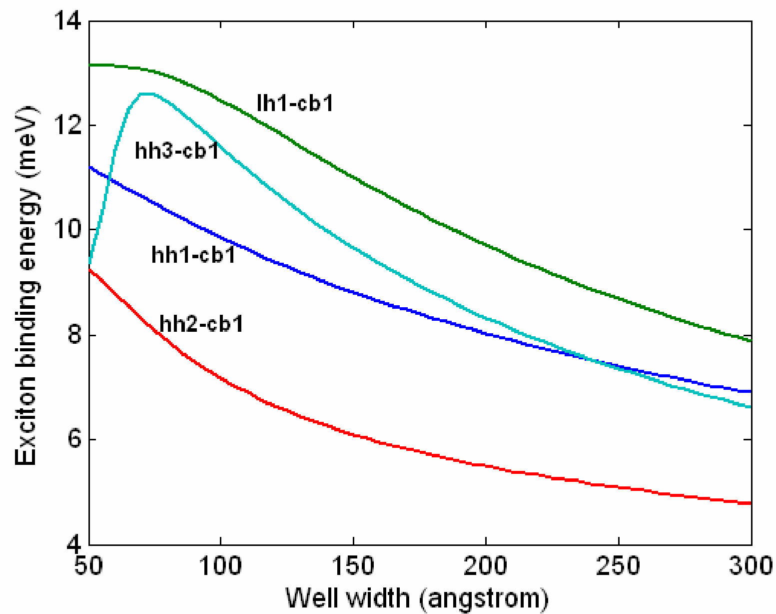

Figure 10. Exciton binding energy versus QW width in a GaAs/AlGaAs SQW (Al mole fraction=0.25).

2.4 Linear optical susceptibility in quantum wells

The susceptibility must account for both the bound (exciton) and the continuum (band-to-band) transitions. They are given as [33]

$$\chi_{cont.}(\omega) = \frac{e^2\hbar}{m_0\omega}\sum_{nm}\sum_{\mathbf{k}_\parallel}\frac{2}{m_0 E_{nm}^d(\mathbf{k}_\parallel)}\left|\boldsymbol{\varepsilon}\cdot\mathbf{p}_{nm}(\mathbf{k}_\parallel)\right|^2\left(\frac{1}{\hbar\omega - E_{nm}^d(\mathbf{k}_\parallel)+i\Gamma}\right),$$

(band-to-band transitions) (13a)

$$\chi_{ex}(\omega) = \frac{e^2\hbar}{m_0\omega}\sum_{l\alpha} f_{osc}^{l\alpha}\left(\frac{1}{\hbar(\omega - E_{ex}^{l\alpha})+i\Gamma}\right),$$

(bound exciton transitions) (13b)

with e the electron charge, $\hbar$ Planck's constant, m_0 the free electron mass, $\boldsymbol{\varepsilon}$ the polarization vector of the light (the optical selection rule is accounted for in the dot product with optical matrix element $\mathbf{p}_{nm}$), $E_{ex}^{l\alpha}$ the eigenenergy of the $l\alpha$-th bound exciton, and Γ a phenomenological dephasing rate of the transitions (described in Section 2.4). The light polarization is assumed to be transverse electric throughout the dissertation. E_{nm}^d is the joint energy dispersion between the n-th conduction and m-th valence subband in the QW. Equation (13) is that obtained from the polarization equation of the semiconductor Bloch equations in the low carrier density limit. For $n \geq 10^9$ cm^{-2}, density effects, such as excitation induced dephasing, come into play. Therefore, our treatment should be valid in the low excitation limit. The optical (momentum) matrix element in the equation is $\mathbf{p}_{nm}(\mathbf{k}_\parallel) = \sum_\nu \mathbf{p}_{c,\nu}^0 I_{nm}^\nu(\mathbf{k}_\parallel)$, where $\mathbf{p}_{c,\nu}^0 = \left\langle U^c \middle|\mathbf{p}\middle| U^\nu\right\rangle$ is the bulk optical interband matrix element at $\mathbf{k}_\parallel = 0$ between the conduction band and the valence band with the spin component ν and $I_{nm}^\nu(\mathbf{k}_\parallel)$ is the $\mathbf{k}_\parallel$ -dependent overlap integral between the n-th conduction- and the ν-spin component envelope of m-th valence-

subband along the growth direction. The oscillator strength of the $l\alpha$-th bound exciton state $f_{osc}^{l\alpha}$ is

$$f_{osc}^{l\alpha} = \frac{2}{m_0 E_{ex}^{l\alpha}} \left| \sum_{v} \boldsymbol{\varepsilon} \cdot \mathbf{p}_{c,v}^{0} \sum_{n,m,k_{\|}} G_{nm}^{l\alpha}(k_{\|}) I_{nm}^{v}(k_{\|}) \delta_{l-v,0} \right|^2 . \quad (14)$$

The oscillator strength of the $l\alpha$-th exciton state in Eq. (14) is attributed to only one of the four spinor components (that makes $l–v$=0 due to the delta function inside the modulus square) that contribute to the exciton envelope function $\Psi_{\alpha,env}^{l}$ in Eq. (8). Summations over n and m in both Eqs. (8) and (14) indicate that mixing of excitons originating in different subband pairs is included in the calculation, which is very important in obtaining accurate optical properties of the ADQWs (discussed in Chapter 3). The detailed theory of the excitons in this context is found in Refs. [12]-[14]. Here, we calculate only s-like excitons that significantly contribute to the absorption spectra. The 2D Sommerfeld factor is multiplied in Eq. (13a) in the calculation to account for the enhancement of the optical transitions at the band edge due to the final-state Coulomb interaction of the exciton continuum states [3]. In the 2D-limit, the oscillator strength at the band edge is twice that of the free-carrier transition and the effect is decreases gradually as the transition energy increases.

Figure 11 shows the overlap integrals $I_{nm}^{v}(\mathbf{k}_{\|})$ between the first conduction-subband envelope and only the major spin components of the four valence-subband envelopes in a GaAs/AlGaAs SQW. If the overlap integrals are assumed to be independent of the wavevector, they will have the same values as at $I_{nm}^{v}(\mathbf{k}_{\|}=0)$. In this assumption, those of *hh2-cb1* and *hh3-ch1* are almost zero, which reflects the selection

rule prohibiting the transitions at zone center. Band-mixing, however, slightly relaxes the selection rule, as the wavevector increases and thus the transitions are weakly allowed. For the accurate estimation of $f_{osc}^{l\alpha}$ and $\chi_{cont.}$, all four spin components, which are nonzero at $\mathbf{k}_{\parallel} \neq 0$, in the valence subbands should be accounted for in the $I_{nm}^{\nu}(\mathbf{k}_{\parallel})$.

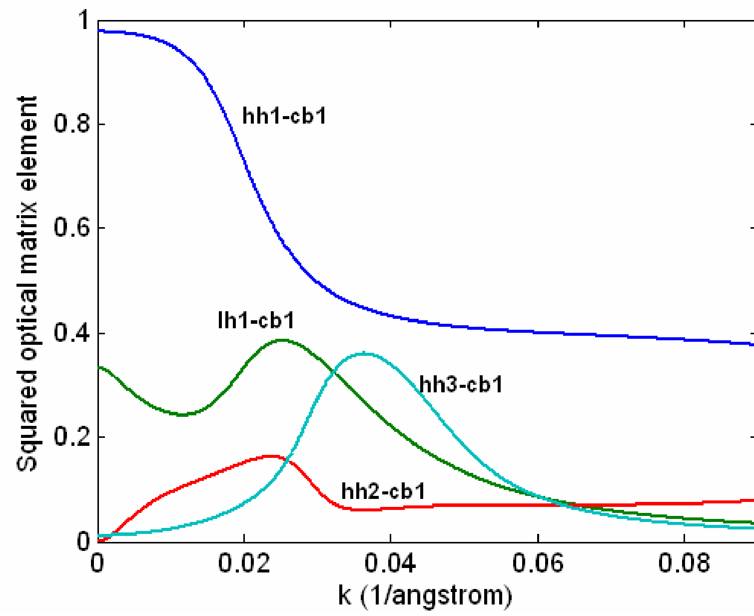

Figure 11. In-plane wavevector dependent overlap integrals between the first conduction subband and the major spin components of the four valence-subband in a 100 Å thick GaAs/$Al_{0.25}Ga_{0.75}As$ QW.

2.5 Line broadenings

The line-broadening in Eq. (13) depends on the applied electric field, especially in QWs with ternary or quaternary alloys, thus strongly affecting the performance of QW-EAMs. Line-broadening can be categorized into two types: homogeneous and inhomogeneous.

Homogeneous broadening is caused by the finite lifetime of the interband excitations due to scattering with phonons, impurities, and other carriers [36], radiative recombination, and field-induced tunneling out of the QWs [47]. At 300 K, the broadening due to scattering with impurities and the carriers [48] may be ignored in the limit of low background doping and low optical excitation; instead, phonon-induced broadening dominates. The full width at half-maximum (FWHM) of the thermal (phonon-induced) broadening is

$$\Gamma_{ph}(T) = \frac{\Gamma_{ph,0}}{\exp(-\frac{\hbar\Omega_{LO}}{k_B T}) - 1}, \tag{15}$$

with $\Gamma_{ph,0}$ the contribution at $T = 0$ K, $\hbar\Omega_{LO}$ the LO-phonon energy, and k_B the Boltzmann constant. $\Gamma_{ph,0}$ depends on the material and dimensionality (2D-GaAs ~ 10 meV, 2D-InGaAs ~ 18 meV, 3D-GaAs ~ 14 meV) [49], and we take the value for 2D-InGaAs for InGaAsP-QWs. The LO-phonon energies for binary compounds are 35.4, 50.09, 42.7, 62.2, 50.7, and 29.6 meV in GaAs, AlAs, InP, AlP, GaP, and InAs, respectively [50], and those of ternary and quaternary alloys can be interpolated linearly from these using Eq. (2). Thermal broadening is considered independent of the applied field. The FWHM associated with field-induced tunneling Γ_T, however, can be strongly bias-dependent even at low electric field depending on the height and the width of the isolating barriers

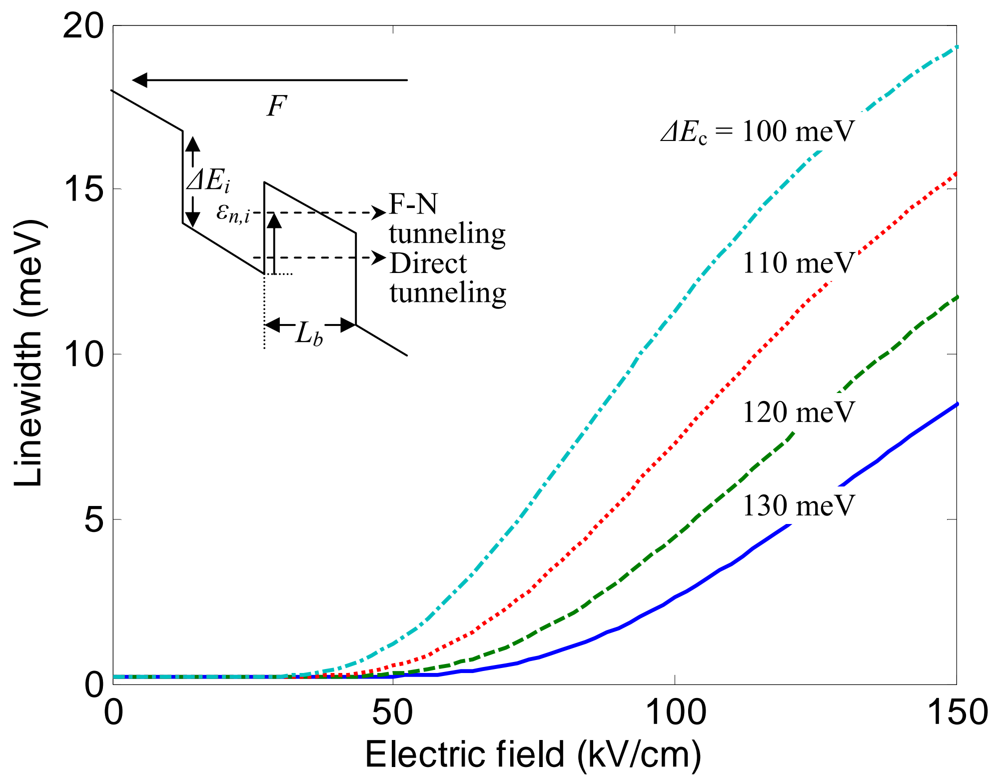

Figure 12. Line-broadening caused by the Fowler-Nordheim (F-N) tunneling of the lowest conduction subband in InGaAsP SQWs (well width ~105 Å) for various conduction offsets as a function of the bias showing that tunneling begins to increase drastically above the direct tunneling regime.

between the QWs. Γ_T is related to the tunneling lifetime τ_T of the carrier by $\Gamma_T = \hbar / \tau_T$. In the limit of strong confinement, the broadening caused by direct tunneling at low bias field (see the inset of Figure 12) is found to be smaller than 0.5 meV and can be safely ignored. As the bias is increased and the lowest barrier height becomes smaller than the subband energy (*i.e.*, triangular barrier), the tunneling probability increases rapidly, following the Fowler-Nordheim model [48]. The tunneling lifetime of a carrier can be calculated using [48],[52]

$$\frac{1}{\tau_{T,n_s,i}} \approx \frac{n_s \hbar \pi}{2 L_w^2 m_{wi}} \cdot \exp\left(- \frac{4\sqrt{2 m_{bi}}\,[\Delta E_i - \varepsilon_{n_s,i}(F)]^{3/2}}{3\hbar \cdot eF} \right), \tag{16}$$

with i the index of the carrier type (electron or hole), n_s the subband index, L_w the width of well, and $m_{w(b)i}$ the effective mass in the well (isolating barrier), respectively. ΔE and ε are the band offset and the energy of the subband in the well and F is the electric field across the barrier. In InGaAsP QWs, electrons usually have much shorter tunneling lifetime than holes do because of the lower effective mass and barrier height. Γ_T's that are induced by the first conduction subband (*cb1*) of a 10.5 nm wide InGaAsP SQW for various conduction-band offsets are calculated and plotted in Figure 12. Equation (16) should be modified if the confining barrier is thin and the broadening induced by direct tunneling is comparable to other broadenings. The electron-hole Coulomb attraction is expected to suppress the effects of Fowler-Nordheim tunneling to some degree; thus, this model offers a quite conservative estimate of the effects of field ionization.

Inhomogeneous broadening is caused by imperfections in the physical structures such as well-width fluctuations and the microscopic compositional variations of the alloys. This broadening mechanism can be treated as independent of temperature, but not

of electric field. In InGaAsP alloy QWs, statistical broadening due to compositional fluctuations, which are mainly caused by the migration and the segregation of P atoms, is large and should be accounted for. We use the experimentally measured statistical broadening Γ_{st} of InGaAsP SQWs [53] that depends on the mole fraction of P atoms of the well layer, which is reproduced in the inset of Figure 13. The broadening due to layer-width fluctuation Γ_{ww} is estimated by calculating the difference of the allowed energies between the original and a structure thicker by one monolayer [54]. Since not only the subband energies shift but also the exciton binding changes as the electric field increases, Γ_{ww} is strongly bias-dependent. Γ_{st} is assumed independent of the bias field. The right inset in Figure 13 shows the field-dependent Γ_{ww} of the 1*s*-like excitons between *cb1* and the four highest valence subbands (*hh1*, *lh1*, *hh2*, *hh3*) in the 10.5 nm wide InGaAsP SQW. The broadening due to the distributed field strengths from layer to layer in the MQW that is induced by the background doping in the intrinsic active region [52] is not considered in this work because when the doping level is less than 5×10^{15} cm^{-3} and the thickness of the active layer is smaller than 0.3 μm, the maximum bias difference in the active layer is found to be less than 0.22 kV/cm. This, however, increases linearly with the doping level, which can be serious if the concentration of the unwanted impurities is poorly controlled in the fabrication process. The actual picture of inhomogeneous broadening is quite complicated as microscopic alloy fluctuations may produce an effective potential landscape for excitons [55] with fluctuations on larger length scales that will also in effect be bias dependent. The total FWHM is obtained by summing all of the above contributions, which is plotted as a function of the bias field in Figure 13.

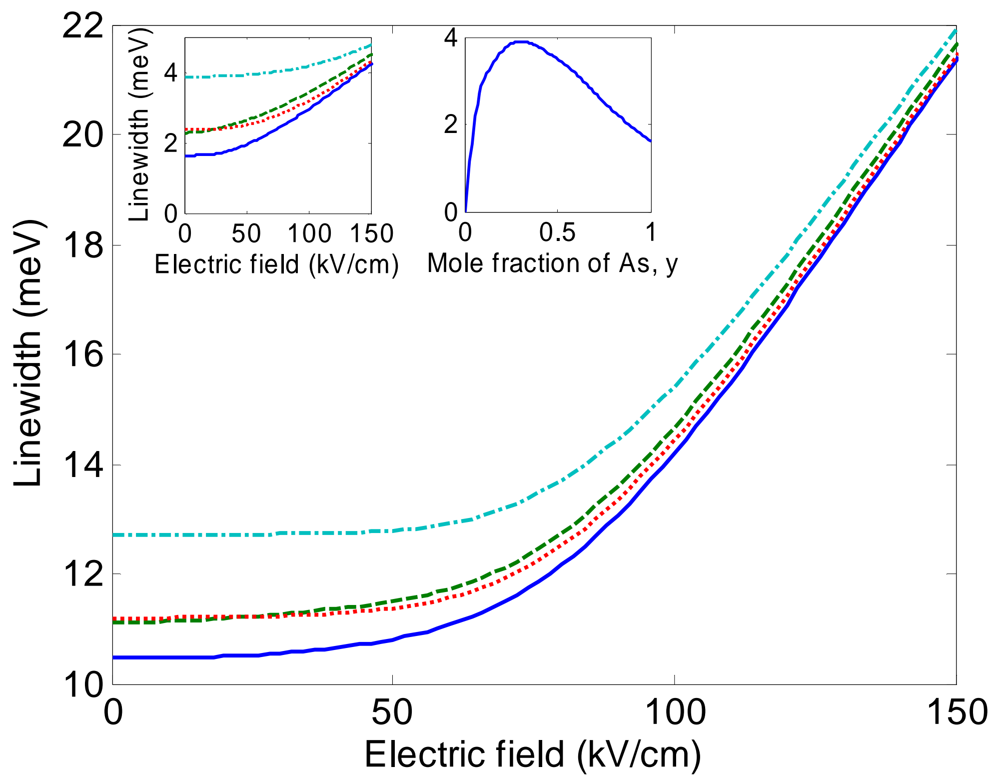

Figure 13. Total line-broadening of the four lowest exciton *1s*-like states as functions of electric field at room temperature in SQW-A (solid: *cb1*-*hh1*, dashed: -*lh1*, dotted: -*hh2*, dot-dashed: -*hh3*). Left inset: line-broadening caused by the well-width fluctuations. Right inset: measured photoluminescence linewidth in an InGaAsP QW as a function of As-mole fraction [53].

CHAPTER 3

ELECTRIC-FIELD-INDUCED MIXING OF EXCITONS IN ASYMMETRIC DOUBLE QUANTUM WELLS

In the introduction, we proposed to adopt ADQWs in enhancing the electroabsorption properties of the QW-EAMs for analog/digital interconnects applications. Extensive band-gap engineering demonstrated that coupled double QW (CDQW) structures could offer enhanced electro-optical properties and thus has been a popular research topic to the present day [21],[22],[28],[43],[48],[56]-[62]. CDQWs exhibit more complicated bias-dependent optical properties than those of SQWs, thus requiring a more careful consideration of effects frequently neglected for SQWs, such as the mixing of excitons originating in different subband pairs. (This should not be confused with the spatial extension of subband envelope wavefunctions from well to well in CDQWs that occurs regardless of the Coulombic mixing of the subband pairs or valence subband mixing.) The mixing of excitons is pronounced when the energy difference between two adjacent excitons is smaller than the typical exciton binding energy, which occurs not only in fairly wide SQWs with weak confinements, but also in some bias range of electric field in CDQWs. VBM affects both the energy levels and the oscillator strengths of excitons through the nonparabolic energy dispersions of the valence subbands and wavevector-dependent overlap integrals between the electron and hole envelope functions, leading to increased accuracy of the theoretical estimates. A convenient way of including the $k_{\|}$-dependences and exciton mixing is via the momentum-space approach that is discussed in the previous chapter.

Early theoretical studies on DQWs, however, did not take full account of VBM, although they included the mixing of excitons in various ways. Bauer *et al.* [63] included only the nonparabolic E-$k_{||}$ dispersions of single particles, *i.e.,* electrons or holes in their calculation, where the excitonic mixing was explicitly included through the off-diagonal matrix elements of the effective-mass Hamiltonian. Lee *et al.* [22] calculated excitonic spectra of ADQWs in electric fields without including the mixing of excitons and VBM, and obtained the fundamental optical properties. Fox *et al*. [64] included the mixing between ground-state excitons in symmetric coupled QWs, where the mixing effects appeared in the exciton wavefunctions as the modifications of the unmixed single-particle subband wavefunctions. They also pointed out that the anticrossing bias field of the two ground-state excitons shifts from that of the corresponding band-to-band transitions due to the exchange of the exciton binding energies. Kamizato *et al.* [43] applied almost-degenerate perturbation theory to the unmixed ground-state excitons to account for the mixing in DQWs. Dignam *et al*. [57] analyzed in detail the four exciton states *e1*-*hh1*, *e1*-*hh2*, *e2*-*hh1*, and *e2*-*hh2* [*en* (*hhm*) refers to the quantized n (m)-th conduction (valence) subband] in symmetric and asymmetric CQWs in a static electric field by employing the variational method and showed that inter- and intra-well transitions strongly mix the radial components of exciton states, which agreed with the results in Ref. [43]. In DQWs with thin coupling barriers, however, the unmixed exciton model was found to yield good agreement with the experimental results [58]. These studies in essence did not require a deeply rigorous treatment of VBM effects because most of the involved excitonic anticrossings were between electron subbands, *i.e.*, between *e1*-*hh1* and *e2*-*hh1*, where VBM does not play an important rôle.

Numerous studies have demonstrated that incorporating an ADQW can yield better performance of QW Stark electro-optic modulators [28],[59],[60] and can lead, further, to the development of new functional devices [61],[62] for practical applications. In ADQWs, utilizing the heavy-hole subband anticrossing (*e1*-*hh1* and *e1*-*hh2*), however, can be advantageous: The effective mass of the heavy hole is in general much greater than that of electrons in type-I QWs, which leads to stronger confinement and thus requires thinner barrier thickness for the same degree of anticrossing effect. This, in turn, can increase the overall absorption efficiency per unit thickness of the device. In addition, the bias field required for the anticrossing of the excitons near the band edge is much smaller than that of electron anticrossings, which potentially reduces the operating bias of the device. However, a complete theoretical analysis of these effects has hitherto not been carried out. This is important since marked discrepancies between theory and experiment may show up in the oscillator strengths whereas the exciton binding energies may be computed with adequate accuracy in an overly simplified model.

In this chapter, we study theoretically the effect of strong mixing of *e1*-*hh1* and *e1*-*hh2* *s*-like excitons on the energy levels and oscillator strengths of excitons within the anticrossing bias range while including VBM rigorously. The effect of mixing is appreciated in two ADQW structures having different degrees of coupling between the two wells through the coupling barrier (CB, thickness ~1.2, 3 nm) by including and excluding the off-diagonal Coulomb matrix elements (between the two different subband pairs) in the effective-mass Hamiltonian for excitons. The validity of the results obtained from these models is discussed in terms of the oscillator-strength sum rule (*f*-sum rule). We find that the *f*-sum rule breaks down in models that ignore exciton mixing, the reason

for which is sought by analyzing the $k_{\|}$-dependent Coulomb matrix element and the corresponding expansion coefficients of the exciton wavefunction. Further, we show that applying almost-degenerate perturbation theory to the two unmixed ground-state excitons obtained from the two-subband model which includes VBM should be carried out with caution in analyzing the electric-field-dependent optical properties of ADQWs, a technique that has often been employed to account for the mixing of excitons.

3.1 Mixing of excitons originating in different subband pairs

We focus on the mixing of the *e1-hh1* and *e1-hh2* excitons, where the major spinor component (v_m=±3/2) of the mixed exciton states remains the same as that of unmixed excitons obtained from the two-subband model, which retains m_l as a good quantum number even after the mixing. However, this is not always true for the mixing of heavy- and light-hole excitons; orbital angular momentum is not a good quantum number because the mixed state is not dominated by only one component.

Because *p*-like states have negligible oscillator strengths (unless they mix strongly to the *s*-like light-hole excitons and m_l is not well defined any more [65]), we consider the mixing of only *s*-like (l=3/2) states of *e1-hh1* and *e1-hh2* excitons in Eq. (10), which yields the 2×2 Hamiltonian matrix to be diagonalized,

$$H^l = \begin{bmatrix} T_{11} + V^l_{11,11} & V^l_{11,12} \\ (V^l_{11,12})^* & T_{12} + V^l_{12,12} \end{bmatrix}, \tag{17}$$

where T_{nm} is the kinetic energy of the n-th electron and m-th hole (to calculate *p*-like states, one only need change l to 1/2). Neglecting exciton mixing is simply to set the off-diagonal element $V^l_{11,12}$=0. Applying the variational approach only to the diagonal element H^l_{11} (H^l_{22}) with an appropriate set of Gaussian basis functions and solving the matrix

eigenvalue equation yields the energy $E_{11(2)}^{l\alpha,UC}$ and expansion coefficient $G_{11(2)}^{l\alpha,UC}(k_{\|})$ of the uncoupled *s*-like ground- and excited-state excitons up to the number of the basis set, as discussed in Chapter 2. When exciton mixing is considered, $V_{11,12}^{l}$ is no longer zero but must be computed, and the corresponding matrix eigenvalue equation yields the energy $E^{l\alpha,C}$ and the expansion coefficients

$$G^{l\alpha,C}(k_{\|}) = C_{11}G_{11}^{l\alpha,C}(k_{\|}) + C_{12}G_{12}^{l\alpha,C}(k_{\|}) \tag{18}$$

of the coupled excitons, where the terms on the right side $C_{11(2)}G_{11(2)}^{l\alpha,C}(k_{\|})$ is interpreted as the amplitude of the contribution of the *e1*-*hh1*(*2*) subband pair to the coupled state $G^{l\alpha,C}(k_{\|})$ and the addition on the right side thus does not mean the simple arithmetic addition of the two terms. Note that $G_{11(2)}^{l\alpha,C}(k_{\|})$ is different from the uncoupled exciton state $G_{11(2)}^{l\alpha,UC}(k_{\|})$.

The mixed excitons can be calculated alternatively by applying almost-degenerate perturbation theory to the uncoupled states, which gives a convenient way to understand the physics of exciton mixing. The uncoupled states of the *e1*-*hh1* and *e1*-*hh2* excitons are evaluated separately as described above. The Coulomb interaction $V_{11,12}^{l}$ is then treated as a perturbation to the uncoupled states. The corresponding matrix to be diagonalized is

$$\begin{bmatrix} E_{11}^{l\alpha,UC} & V_{11,12}^{l} \\ (V_{11,12}^{l})^{*} & E_{12}^{l\alpha,UC} \end{bmatrix}, \tag{19}$$

where the Coulomb matrix element $V_{11,12}^{l}$ is evaluated by using the obtained uncoupled states:

$$V_{11,12}^{l\alpha\alpha'} = \sum_{\mathbf{k}_\parallel \mathbf{k}'_\parallel} G_{12}^{l\alpha',UC^*}(k'_\parallel) V_{11,12}^{l}(k_\parallel, k'_\parallel, \varphi') G_{11}^{l\alpha,UC}(k_\parallel) . \quad (20)$$

The corresponding mixed state is then obtained as

$$G_{ADP}^{l\alpha}(k_\parallel) = \sum_{\alpha'} \left(C_{l\alpha,11} G_{11}^{l\alpha',UC}(k_\parallel) + C_{l\alpha,12} G_{12}^{l\alpha',UC}(k_\parallel) \right), \quad (21)$$

where the coefficients $C_{l\alpha,11(2)}$ are the components of the eigenvectors obtained from the diagonalization of Eq. (19), which are the portions of the contribution of the uncoupled states to the mixed ones. Note that Eqs. (18) and (21) are not the same. The oscillator strengths of the mixed excitons can be obtained using the general expression Eq. (14).

3.2 Analysis of exciton mixing in ADQWs

We first analyze two ADQWs having different degrees of coupling of the two wells in the excitonic anticrossing bias range and show that the *f*-sum rule breaks down dramatically if exciton mixing is neglected. This is followed by a detailed investigation of the excitonic-mixing effect on the oscillator strengths and energy levels. We also discuss that almost-degenerate perturbation theory can be misleading if carelessly applied.

3.2.1 Effect of exciton mixing in strongly and weakly coupled ADQWs

The effects of *e1-hh1* and *e1-hh2* exciton mixing in an anticrossing bias range are investigated in two ADQW samples notated ADQW-30 and ADQW-12 which consist of 3 and 1.2 nm thick $Al_{0.25}Ga_{0.75}As$ coupling barriers, respectively, and two GaAs wells (widths ~6.5 nm and ~3.5 nm). The mole fraction of the confining walls is the same as that of the coupling barrier. The material parameters are adopted from Ref. [12].

The mixing is strong in ADQW-30 because the energy difference between the ground states of the *e1-hh1* and *e1-hh2* excitons becomes much smaller than the exciton

binding energy in this sample, as shown in Figure 14(a). The energy differences between the band-to-band transitions (dotted) and the coupled lowest two excitons (solid) can be interpreted as the exciton ground-state binding energies. As stated in Ref. [64], the band-to-band transition energies (energy difference between the electron and the hole subbands at k=0) anticross at much lower bias (~25 kV/cm) than that of the coupled excitons (~31 kV/cm), both very sharply over very narrow bias ranges due to the thick coupling barrier. The binding energies, however, are exchanged gradually from ~25 kV/cm to ~31 kV/cm. This implies that severe mixing of excitons as well as VBM between the *hh1* and *hh2* subbands occur in this bias range. In Figure 14(a), the uncoupled exciton energies (dashed), however, do not even anticross, showing the change of the binding energy at the anticrossing bias of the band-to-band transitions due to the neglect of the mixing effect, which is incorrect.

The corresponding oscillator strengths of the uncoupled and coupled states are shown in Figure 14(b),(c). The transfer of oscillator strength from the *e1*-*hh1* to the *e1*-*hh2* ground-state excitons occurs around ~25 kV/cm and ~31 kV/cm in the uncoupled and coupled cases, respectively. Moreover, the sum of the oscillator strengths of the two uncoupled states [dashed curves in Figure 14(b)] is not uniform in the anticrossing bias range, while this is not so in the coupled case. (The reason for the breakdown of the *f*-sum rule in the uncoupled case will be discussed later in this section.) The minimum of the sum of the oscillator strengths in the uncoupled case at 25.3 kV/cm is only 45 % of the summed value outside the anticrossing range as shown in Figure 14(b).

Figure 14(d) shows that the oscillator strength $f^{1s,C}$ of the coupled ground state has a major contribution from the *e1*-*hh1* (dotted with marks) subband pair until the bias

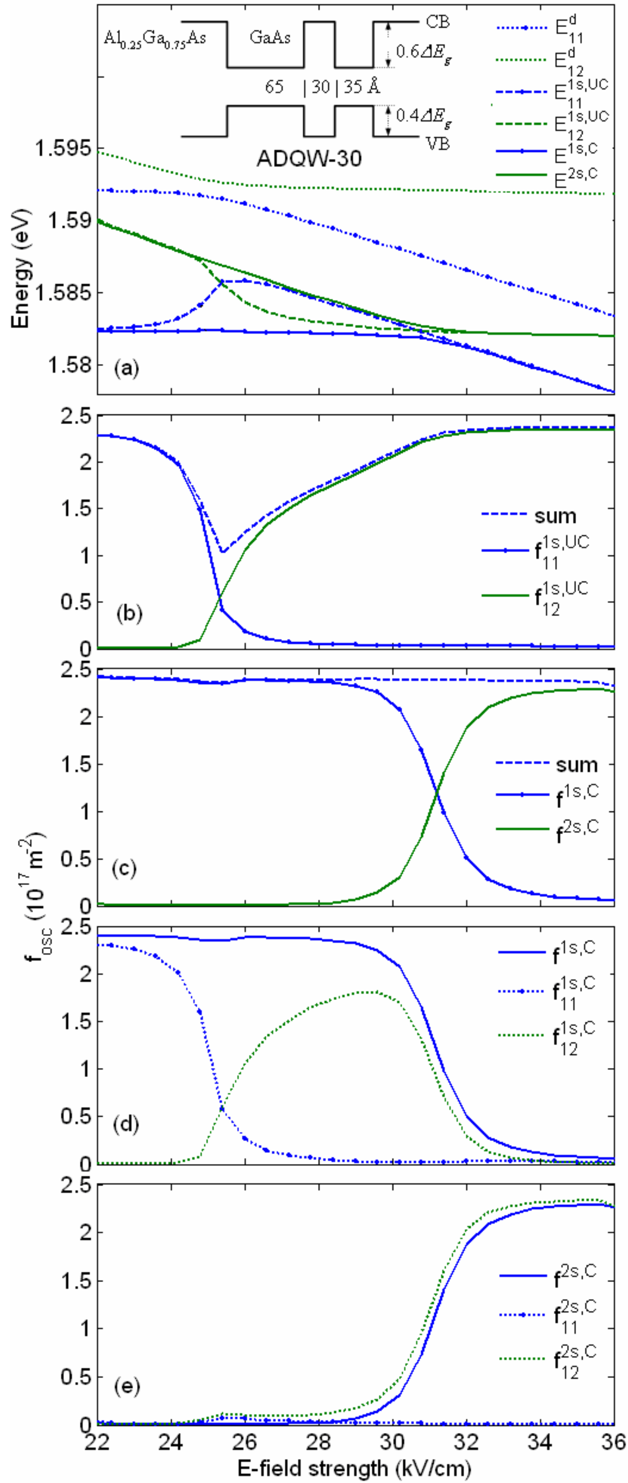

Figure 14. Energy levels and oscillator strengths of excitons in ADQW-30 as a function of the bias field strength. The inset in (a) is the band-edge diagram along the growth direction. (a) Energy levels (solid: couple excitons $E^{\alpha s,C}$, dashed: uncoupled ground-state excitons $E_{11(2)}^{1s,UC}$, dotted: band-to-band transitions $E_{11(2)}^{d}$. *e1-hh1* excitons have dots on the curves). Oscillator strengths of (b) uncoupled ground-states $f_{11(2)}^{1s,UC}$ (c) coupled ground- and excited-state excitons $f^{\alpha s,C}$ (solid) and their sum (dashed). Oscillator strengths of the coupled (d) ground- and (e) first excited-state excitons (solid) and the contributions from *e1-hh1* (dotted with marks, $f_{11}^{\alpha s,C}$) and *e1-hh2* (dotted, $f_{12}^{\alpha s,C}$) subband pairs.

reaches ~25 kV/cm following which the *e1-hh2* (dotted) subband pair contribute the majority, which maintains $f^{1s,C}$ uniform until the bias reaches just below ~31 kV/cm [$f_{11}^{1s,C}$ and $f_{12}^{1s,C}$ are obtained from Eq. (14) by taking the modulus square of *nm*=11 and *nm*=12 separately instead of summing up in advance, which are not physically measurable; this is adopted only to show the portion of the contribution of each subband pair to the coupled states]. Figure 14(e) shows that the oscillator strength of the *e1-hh2* ground-state exciton may be slightly overestimated when only $f_{12}^{2s,C}$ is accounted for [the sum of the contributions from the two subband pairs (*e1-hh1* and *e1-hh2*) in the modulus square of Eq. (14) is smaller than that of only *e1-hh2* subband pair]. Figure 15 shows the actual absorption spectra of an ADQW with a thick coupling barrier that are calculated with and without the inclusion of Coulombic interaction between the two lowest excitons at low temperature.

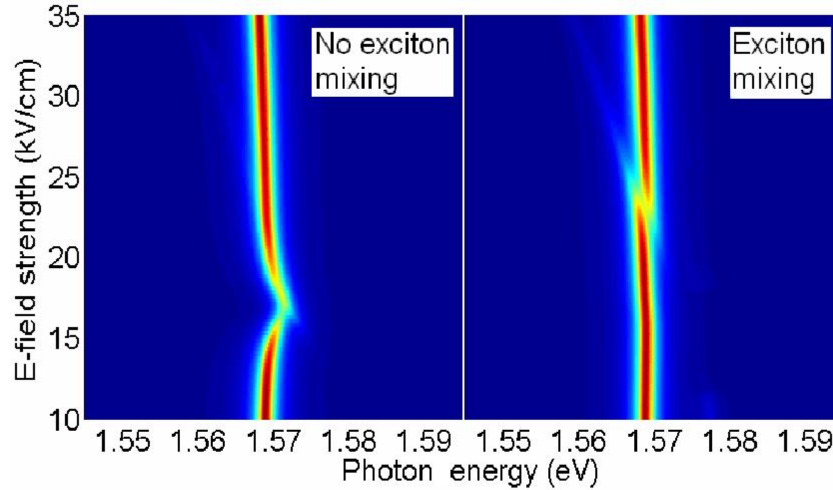

Figure 15. Absorption spectra in the anticrossing bias range calculated with (right) and without (left) the inclusion of exciton mixing effects in an ADQW with BW ~ 21 Å.

The mixing effect is expected to be weak in ADQW-12 because the minimum difference of the band-to-band transition energies in the anticrossing bias range is ~7 meV, which is almost the same as the binding energies of the uncoupled ground-state excitons at the same bias ~33 kV/cm, as shown in Figure 16(a). The energy differences before (dashed) and after (solid) the inclusion of coupling are less than 1 meV in both *e1-hh1* and *e1-hh2* ground-state excitons. The minimum of the sum of the oscillator strengths in the uncoupled case, however, is only 66 % of the expected value [Figure 16(b)], which is substantial, while the *f*-sum rule is conserved in the coupled case as shown in Figure 16(c). This shows that weak coupling in terms of the energy level can still have substantial effect on the oscillator strength. In Figure 16(c), the oscillator strength of the first excited state is transferred to the higher excited states sequentially as the bias increases, which is due to the coupling of the uncoupled *e1-hh1* excited states and the *e1-hh2* ground state.

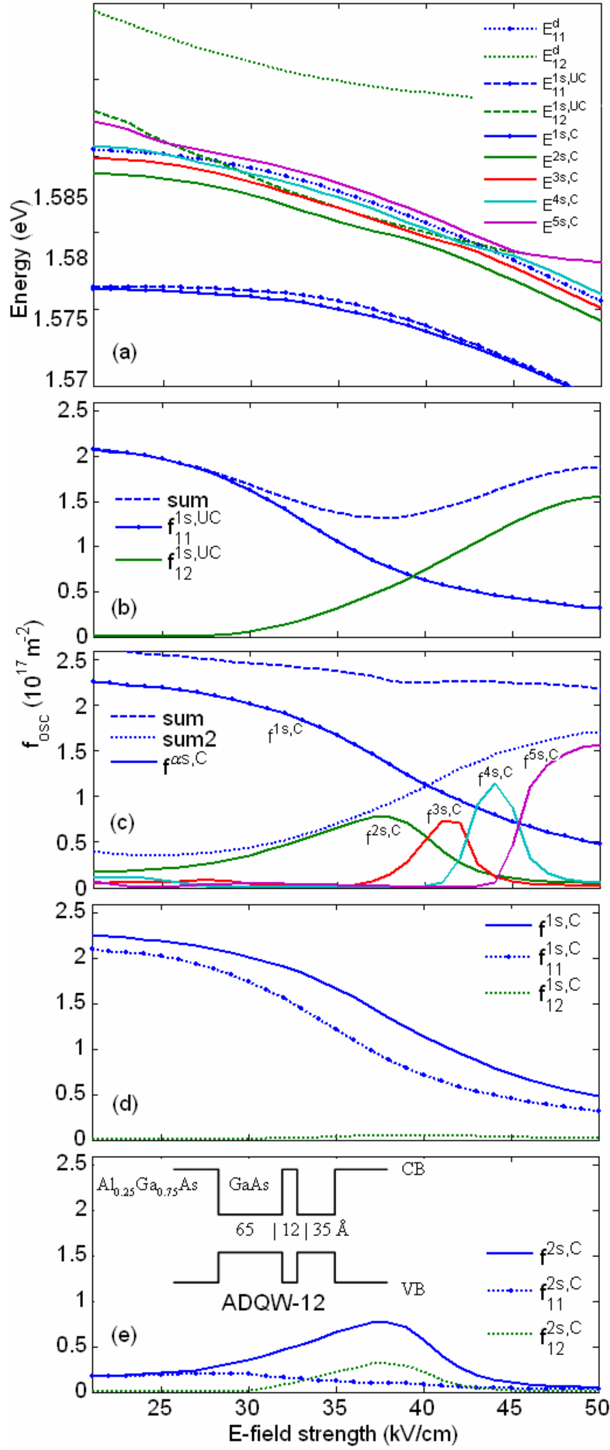

Figure 16. Energy levels and oscillator strengths of excitons in ADQW-12 as a function of the bias field strength. (a) Energy levels of excitons (solids from the lowest to highest: from ground to fourth coupled excitons $E^{\alpha s,C}$, lower dashed: $E_{11}^{1s,UC}$, upper dashed: $E_{12}^{1s,UC}$). Oscillator strengths of (b) uncoupled ground-state excitons $f_{11(2)}^{1s,UC}$ (solid) and their sum (dashed) and (c) coupled excitons $f^{\alpha s,C}$ up to fourth excited states (solid), their sum (dashed: total sum, dotted: sum except $f^{1s,C}$, which shows the sequential transfer of oscillator strength to higher state). (d) and (e) are the same as those in Figure 14.

3.2.2 Analysis in the in-plane wavevector space

The mixing of excitons is attributed to the Coulomb interaction of the excitons, which appears in the off-diagonal elements in Eq. (17) and (19). In the following, we discuss the effect of the terms on the exciton envelope functions and the corresponding oscillator strengths. We pick a bias field of ~26 kV/cm in ADQW-30 that exhibits strong excitonic mixing.

The valence-subband dispersion is plotted in Figure 17(a), where the *hh1* and *hh2* subbands are seen to anticross at ~0.15 nm^{-1} (vertical dotted line). Figure 17(b) shows the Coulomb matrix elements as functions of $k_{\|}$ that are obtained from Eq. (11) by taking the integral along φ' and putting $k'_{\|}=0$, which shows the approximate trend of the $k_{\|}$-dependent Coulomb interaction [in the calculation, the full two-dimensional ($k'_{\|}$, $k'_{\|}$)-dependence should be considered]. The diagonal elements ($V_{11,11}$, $V_{12,12}$) have their largest values near $k_{\|}=0$ and decrease gradually until the two subbands anticross following which they decrease more rapidly and fall to zero. Thus, the resulting $k_{\|}$-dependent $G_{11}^{1s,UC}$ for the uncoupled ground-state exciton originating in the *e1-hh1* subband pair, for example, has very little contribution after the anticrossing $k_{\|}$ value, as shown in Figure 17(c). This leads to the negligible oscillator strength integrand $GI_{11}^{1s,UC}$ in the corresponding $k_{\|}$ range [solid line in Figure 17(d)], where $GI_{nm}^{l\alpha}$ represents the integrand $G_{nm}^{l\alpha}(k_{\|})I_{nm}^{v}(k_{\|})$ in Eq. (14). On the other hand, the off-diagonal element $V_{11,12}$ that represents the Coulomb interaction between the *e1-hh1* and *e1-hh2* subband pairs begins to increase from zero at $k_{\|}=0$ and reaches its maximum at the value of $k_{\|}$ near the anticrossing, which exceeds $V_{11,11}$ in this sample at the given bias field. This means that

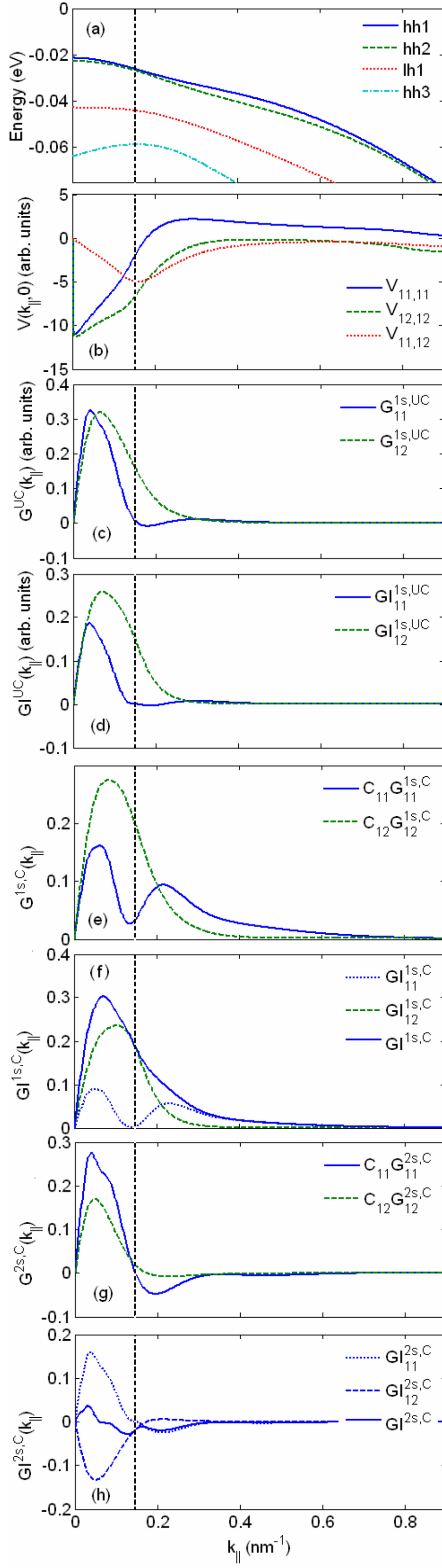

Figure 17. (a) Energy dispersions of four highest valence subbands, (b) one dimensional diagonal and off-diagonal Coulomb matrix elements, (c) expansion coefficients of uncoupled ground-state excitons, (d) integrands of oscillator strengths of uncoupled ground-state excitons in Eq. (6), (e) components of coupled ground-state exciton in Eq. (8) and (f) the corresponding integrands of oscillator strengths (dotted and dashed) and their sum (solid), (g) components of coupled first excited-state exciton in Eq. (8) and (h) the corresponding integrands of oscillator strengths (dotted and dashed) and their sum (solid) as a function of the in-plane wavevector in ADQW-30 at the bias field of ~26 kV/cm. Vertical dotted line indicates the wavevector where *hh1*- and *hh2*- subbands anticross.

the Coulomb coupling of the *e1*-*hh2* to the *e1*-*hh1* subband pair is larger than the Coulomb interaction between the *e1* and *hh1* subbands. As a result of the coupling, the lowest exciton expansion coefficients $G^{1s,C}$ is expressed as a mixture of the basis $G_{11}^{1s,C}$ and $G_{12}^{1s,C}$ whose $k_{\|}$-dependent profiles significantly differ from the uncoupled expansion coefficients $G_{nm}^{1s,UC}$. The basis $G_{11(2)}^{1s,C}$ for the coupled states in Figure 17(e) retains substantial values even after the anticrossing $k_{\|}$ while $G_{nm}^{1s,UC}$ in Figure 17(c) does not. Consequently, the overall value of $GI^{1s,C}$ of the coupled ground state in Figure 17(f) that is obtained by adding $GI_{11}^{1s,C}$ and $GI_{12}^{1s,C}$ has a significantly larger contribution than the sum of the uncoupled ones [$GI_{11}^{1s,UC}$ and $GI_{12}^{1s,UC}$ in (c)] after the anticrossing $k_{\|}$ value. By following the same procedure, the coupled first excited state $G^{2s,C}$ that corresponds to the uncoupled *e1*-*hh2* ground-state exciton is found to have negligible oscillator strength as shown in Figure 17(h).

In summary, neglecting the Coulomb coupling between different subband pairs in a sample that exhibit strong VBM results in the diminish of the contribution of the $k_{\|}$-dependent subband pairs after the anticrossing $k_{\|}$ value, which in turn leads to the underestimation of the oscillator strength, breaking the *f*-sum rule.

3.2.3 Almost-degenerate perturbation theory

Almost-degenerate perturbation theory was applied to the uncoupled states of ADQW-30 to account for the mixing of excitons. In this case, the mixed states are expressed as a linear combination of the uncoupled states as shown in Eq. (21). Employing the two uncoupled ground states $G_{11}^{1s,UC}$ and $G_{12}^{1s,UC}$ only as a basis set for the

purpose of obtaining the coupled ground and first excited states, however, did not yield sufficiently accurate energy levels or oscillator strengths, as shown in Figure 18(a) and (b); the sum of the oscillator strengths is exactly the same as that of the uncoupled ground states due to the unitarity of the transformation to diagonalize the perturbation matrix (see Appendix B). It is found that incorporating only the *ground states* of the uncoupled excitons obtained by including VBM as a basis set is insufficient to account accurately for the strongly mixed exciton states (however, neglecting the VBM [*i.e.*, assuming constant effective mass] and incorporating the uncoupled ground states may yield valid but approximate results [43],[64]). The same results as those obtained from the full mixing model were obtained by incorporating up to ten excited uncoupled states as shown in Figure 18(e). The results in Figure 18(c) and (d), obtained by using only two ground states, however, show that in the bias range from ~25 to ~31 kV/cm the majority of the oscillator strength in the lowest exciton state is attributed to the uncoupled upper ground-state exciton $G_{12}^{1s,UC}$ as a result of strong mixing between the two uncoupled ground-state excitons caused by the Coulomb interaction.

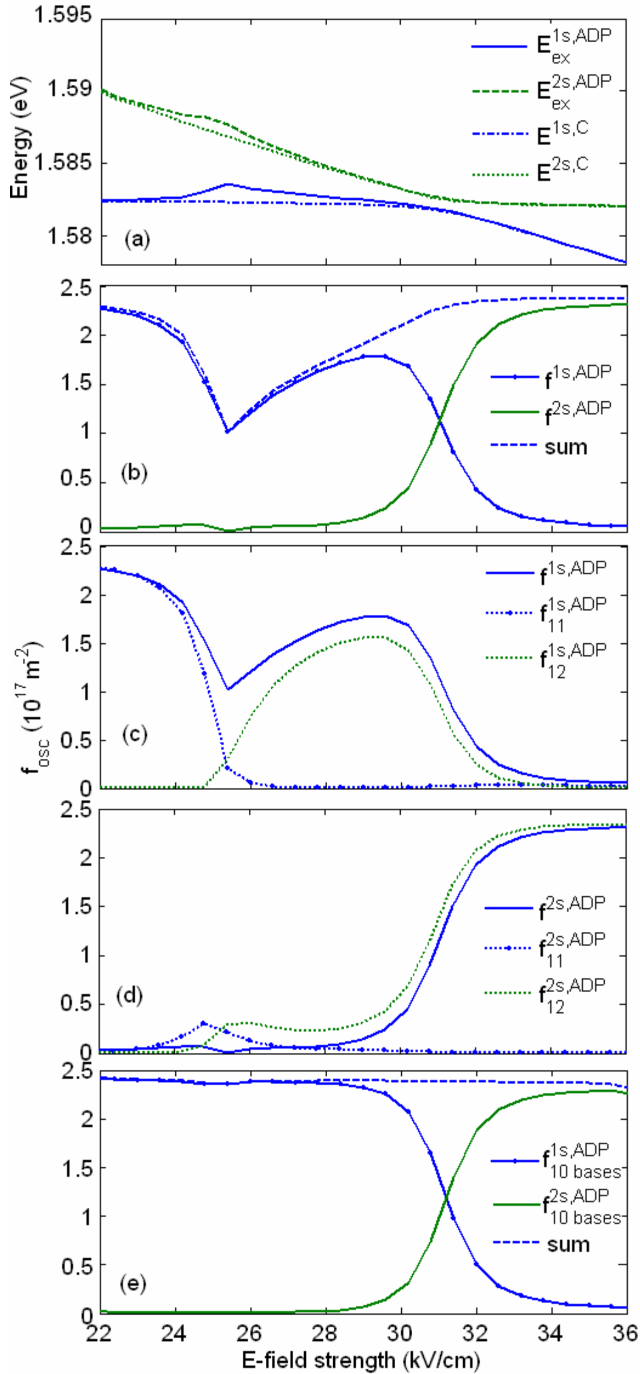

Figure 18. Bias-dependent energy levels and oscillator strengths of excitons in ADQW-30 that are obtained from the almost-degenerate perturbation (ADP) theory. (a) Energy levels of excitons obtained by ADP with two bases $E_{ex}^{\alpha s,ADP}$ that show notable deviation from $E^{\alpha s,C}$. Oscillator strengths of coupled excitons (solid) from ADP with (b) two bases and (e) ten bases and their sum (dashed). Oscillator strengths of the coupled (c) ground-state and (d) first excited-state excitons from ADP with two bases (solid) and the contributions to it from *e1-hh1* (dotted with marks) and *e1-hh2* (dotted) subband pairs.

CHAPTER 4

OPTIMIZATION OF ASYMMETRIC DOUBLE QUANTUM WELLS

In the proceeding chapters, we reviewed the theories required to obtain the linear optical susceptibility of the semiconductor QWs around the band edge and to optimize the ADQW band structures. In the introduction, we proposed to adopt ADQWs as a way of enhancing the modulation sensitivities of the QW-EAMs for analog/digital interconnects applications based on the numerous reports. In this chapter, we analyze the main reason of the enhanced QCSE and discuss the optimization of the structural parameters of ADQWs. We adopt the GaAs/AlGaAs QWs and assume that there is only thermal broadening, which greatly simplifies the analysis and shows clearly the dependences on the structural parameters.

4.1 Enhanced QCSE in ADQWs

QCSE, the basic operating principle of the QW-EAM, has been reported to be enhanced by adopting the asymmetric QWs. This enhancement stems from the anticrossing of the two lowest ground-state (*i.e.*, *s*-like) excitonic peaks near the band edge, which is in essence the result of the anticrossing of the two subbands nearest the band edge in either the conduction or valance band. More specifically, there is an electric-field range in which the spatial location of one of the relevant subband states shifts rapidly with field from one side of the AQW to the other (see Figure 19). ADQWs further enhance such effects over graded SQWs or step QWs, where the former typically involves stronger excitonic mixing in the anticrossing bias range than the latter.

The calculated absorption spectrum and the sensitivity spectrum of a typical ADQW consisting of a 10 Å thick $Al_{0.25}Ga_{0.75}As$ barrier and 65 Å and 35 Å wide GaAs wells are plotted in Figure 19. The two lowest conduction subbands (*cb1*and *cb2*) and the four highest valence subbands (*hh1*, *hh2*, *lh1*, and *hh3*) were included in the calculation, yielding eight observable *1s*-like exciton peaks in Figure 19(a). One notes that the two lowest exciton peaks (*hh1-cb1* and *hh2-cb1*) anticross at the bias field of ~40 kV/cm, which is the result of the anticrossing of *hh1* and *hh2* valence subbands. The maximum $d\alpha/dE$ thus is found at the same bias field, as seen in the dotted circle in Figure 19(b). Figure 20 shows the subband envelopes at different bias fields. At zero bias [Figure 20(a)], most of the *hh1* (*hh2*) envelope lies in the wide (narrow) well, whereas considerable part of *cb1* envelope still remains in the narrow well due to the smaller effective mass and band-offset ratio of the conduction band. As the bias increases from zero, the oscillator strength of the lowest exciton (*hh1-cb1*) increases and its energy level blue-shifts due to the increased overlap integral of *hh1* and *cb1* envelopes and the corresponding increase of the exciton binding energy [Figure 20(b)] until *hh1* subband moves to the narrow well, which we call the critical bias field. Thereafter, a large red-shift is observed due to the rapid reduction of the energy difference between *hh1* (in the narrow well) and *cb1* (in the wide well) subbands while still keeping observable oscillator strength caused by the *cb1* envelope that is confined in the wide well [Figure 20(c)].

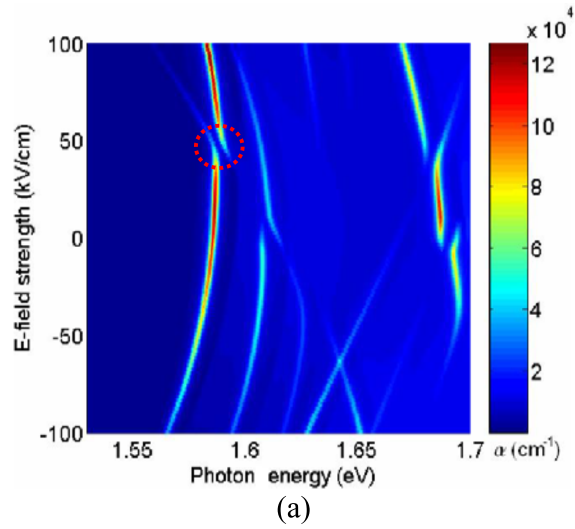

(a)

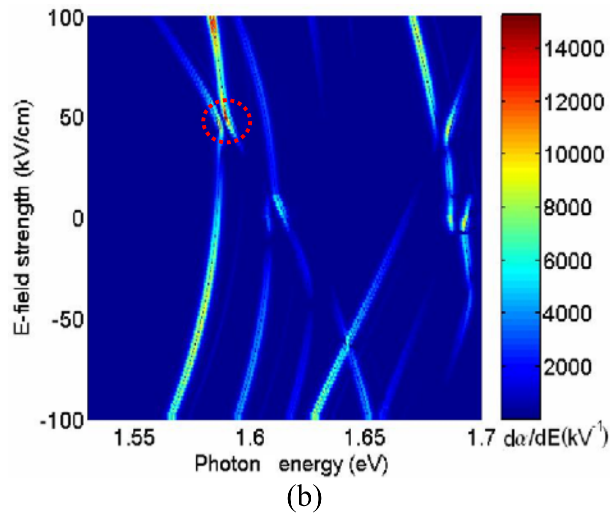

(b)

Figure 19. (a) Absorption coefficient spectra of an ADQW as a function of the applied electric field and photon energy. The FWHM of the Lorentzian function is 2 meV. The anticrossing of *hh1-cb1* and *hh2-cb1* exciton is shown in the dotted circle. (b) Modulation sensitivity spectra obtained by taking the partial derivative of the absorption coefficient (a). The maximum sensitivity is observed in the dotted circle where the two lowest excitonic states anticross.

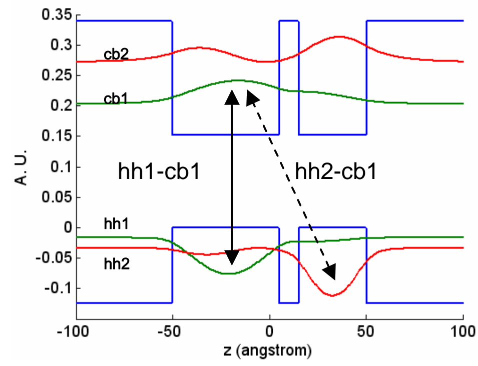

(a)

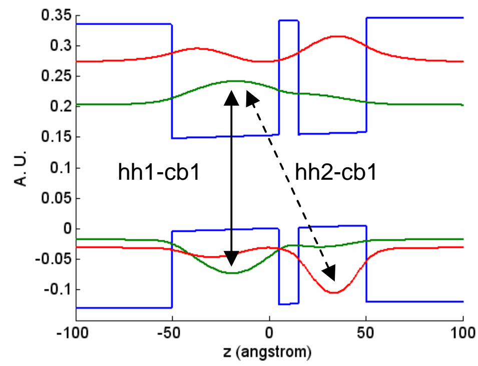

(b)

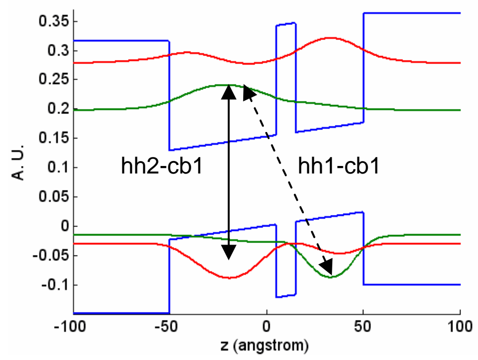

(c)

Figure 20. Subband envelopes at (a) zero bias, (b) 40 kV/cm (before anticrossing), and (c) 60 kV/cm (after anticrossing).

4.2 Optimization of ADQWs

We focus on the dependence of the maximum modulation sensitivity on various parameters of the ADQW: BW, barrier position (BP, distance from the QW center), overall WW, and the FWHM of the Lorentzian line-broadening function [37]. The band-edge diagram of an arbitrary ADQW is drawn in Figure 21. The well material is GaAs and the middle barrier and the confining walls are $Al_xGa_{1-x}As$ with x ~0.25. The band-offset energy is calculated from $\Delta E_g = 1.155x+0.37x^2$ and the ratio between conduction and valence band offsets is assumed 0.6/0.4.

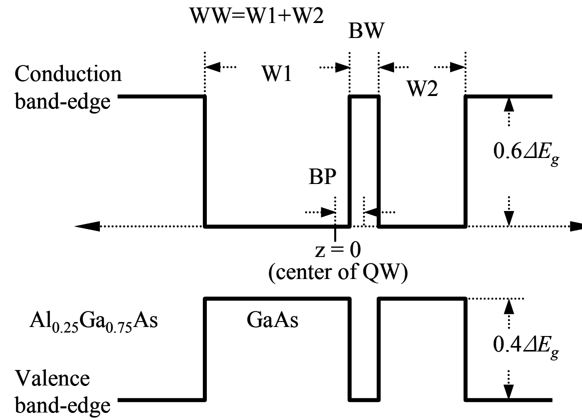

Figure 21. Band-edge diagram of an ADQW composed of the two GaAs wells coupled through a $Al_{0.25}Ga_{.0.75}As$ middle barrier and the confining walls having identical composition to the middle barrier.

Figure 22 shows the dependence of the maximum sensitivity on the BW and the FWHM. The BP and the overall WW are fixed at 10 Å and 100 Å, respectively. When the BW is very small (or even zero), the anticrossing of the lowest two heavy-hole subbands occurs over a very wide bias range yielding an overall QCSE similar to that of

the SQW. As the BW is increased, the sensitivity increases up to a maximum because of the more abrupt anticrossing of the lowest two exciton states over a narrower bias range caused by stronger repulsion of the states induced by the stronger coupling between them. Heuristically, a very thick barrier should separate the two wells so greatly to the extent they do not couple and behave as independent SQWs yielding the QCSE of the two SQWs with different WWs. This was observed in our simulation result; as the BW increases from zero, the maximum sensitivity reaches maximum at 23 Å and then decreases for the FWHM of 1 meV in Figure 22. It is also natural that the maximum sensitivity decreases as the FWHM increases, because the absolute value of the absorption coefficient caused by the broadening of the excitonic peaks decreases. However, the BW that maximizes the sensitivity also decreases as the FWHM increases, as observed in Figure 22. When the BW increases, the energy difference of two lowest exciton states becomes smaller in the anticrossing bias range because of the decrease of the energy difference between the *hh1* and *hh2* valence subbands. As the energy difference of the two lowest exciton states becomes smaller than the FWHM of the absorption peaks, the two excitonic features begin to overlap yielding the decrease in the sensitivity as the BW increases further. For example, for the FWHM of 1 (3, 5) meV in Figure 22, the maximum sensitivity reaches its greatest value at the BW of 23 (18, 12) Å and thereafter decreases, which means that the energy difference of the two anticrossing exciton states is about 1 (3, 5) meV at the bias point where the maximum sensitivity is found. The maximum sensitivities are 6.5×10^4 kV^{-1} and 1.2×10^3 kV^{-1} with FWHM of 1 meV (4.2 K) and 7 meV (298 K) and BWs of 24 Å and 12 Å, respectively.

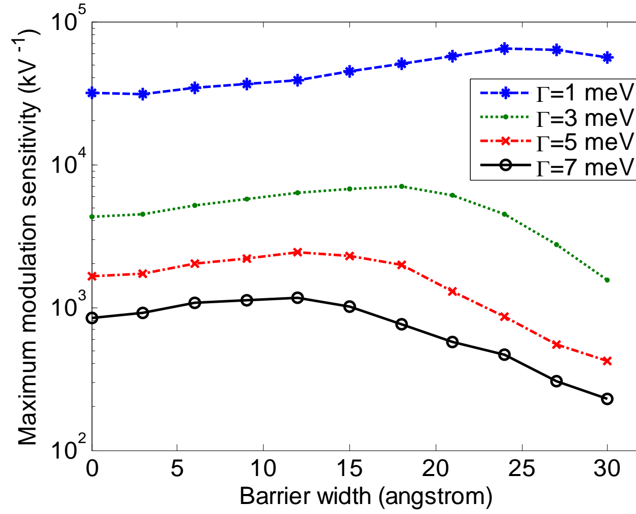

Figure 22. Maximum absorption coefficient modulation sensitivity as a function of the barrier width and FWHM (Γ) of the exciton peaks.

Figure 23 shows the dependence of the maximum sensitivity on the BP, which is equivalent to the degree of asymmetry of the DQW. The BW and the overall WW are fixed at 12 Å and 100 Å, respectively. As the BP becomes offset from the center of the QW, the sensitivity attains its maximum at some point following which it falls off. This is also because of the increase of abruptness of the anticrossing up to this point. When the barrier is close to the side of the QW and one well becomes so narrow that the lowest subband in that well lies at considerably higher energy, the ADQW assumes the properties of a SQW, which is the reason for the decrease of the sensitivity. Apparently, the degree of the asymmetry of the DQW is an important parameter in enhancing the sensitivity, but its dependence is not as significant as that on the BW. The BP that maximizes the sensitivity did not show notable change as the FWHM increases. The maximum sensitivities are 4.48×10^4 kV^{-1} and 1.25×10^3 kV^{-1} with FWHM of 1 meV and 7 meV, respectively, and BP of 15 Å.

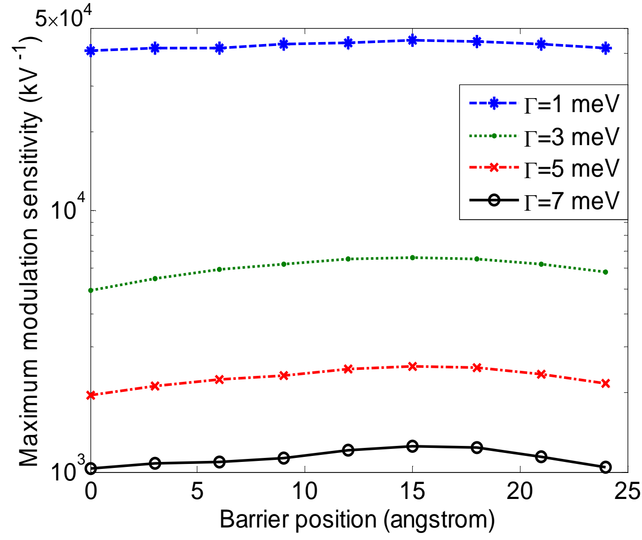

Figure 23. Maximum absorption coefficient modulation sensitivity as a function of the barrier position and FWHM (Γ) of the exciton peaks.

The dependence of the sensitivity on the overall WW with fixed BW and ratio of the two wells at 12 Å and 3:2, respectively, was also investigated. The overall WW was changed from 50 Å to 180 Å. When the overall WW decreased below 70 Å, the anticrossing of the two lowest exciton states did not significantly enhance the modulation sensitivity, just showing that of an asymmetric SQW, because the energy difference of the two lowest heavy-hole states was so large (> 20 meV) that the two states did not interact strongly. As the WW was increased, the two lowest exciton levels became closer and interacted more strongly resulting in the increased modulation sensitivity. However, when the WW was increased beyond 150 Å, not only the lowest two exciton states became closer, but also the other higher states were close enough to overlap with the lowest two excitonic states resulting in the decrease of the sensitivity and, in the case of

large FWHM, the blurring of the overall absorption spectra and sensitivity spectra, which looks like those of the continuum state.

In summary, the BW, the BP, and the WW of ADQWs are optimized theoretically to exhibit maximum modulation sensitivity, which provides the design guidelines in fabricating high-sensitivity QW-EAMs. For sufficiently high quality QWs, the dependence on the FWHM of the exciton peaks can be mapped onto temperature. However, caution is required in generalizing this interpretation, because the FWHM may also be sensitive to the applied bias, the quality of the heterojunction interfaces, and the uniformity from QW to QW within a sample. In this work, each of the three parameters – BW, BP, and WW – are optimized independently by fixing the other two parameters at the intuitively chosen values. The sensitivity may be improved further by optimizing these parameters collectively using a multivariate optimization algorithm [66].

CHAPTER 5

ELECTROOPTIC PROPERTIES OF InGaAsP-BASED ASYMMETRIC DOUBLE QUANTUM WELLS

Quantum-well (QW) electroabsorption modulators (EAMs) are considered most suitable for applications in analog optical fiber links especially because of their superb modulation efficiency and small size compared with several other types of optical modulators [1]. Among them, InGaAsP-based QW-EAMs are popular due to the feasibility of operating at ~1550 nm, integration with other devices, and mature fabrication technology [2]. There are two types of QW-EAMs depending on the propagation direction of the light through the QW: normal incidence and waveguide types. For high speed operation, the waveguide type is preferred because not only the light propagates along the optical waveguide, but also the electrical field that modulates the light can be designed to travel along the electromagnetic waveguide electrodes, which facilitates the high frequency operation. Recently, a traveling waveguide InP-based QW-EAM operating above 20 GHz for analog applications was reported to exhibit high modulation efficiency at low driving voltage while keeping other parameters comparable with those of the conventional ones [30]. The device adopted multiple layers of single QWs (SQWs) as the active absorptive layers.

In the preceding chapter we optimized only the potential structures of an ADQW that maximizes the modulation sensitivity of the absorption coefficient rather than optimizing the performance of the real device–QW-EAM. In this chapter, we adopt a InGaAsP-based waveguide-type single QW-EAMs [67] that was studied experimentally

and was found to exhibit the best modulation efficiency; we therefore adopt this as a test case, and reproduce the experimental transmission data theoretically by using our model. Further, we show that the modulation efficiency, which is one of the most important figures-of-merit in the analog optical fiber link application, can be enhanced considerably by employing an optimized ADQW. To simplify the problem, the optimization of the ADQWs was carried out on only one parameter, the middle barrier width, which was shown to be most important in Chapter 4.

5.1 Transmission in SQW-EAMs

5.1.1 Modeling the transmission of waveguide EAMs

The optical power transmitted through an EAM in a waveguide geometry can be modeled as

$$T = \Gamma_c (1 - R) \exp(-\gamma \alpha L),$$

where Γ_c is the coupling loss to the modulator, R is the reflectance at the interface, γ is the optical confinement factor, α is the absorption coefficient, and L is the interaction length of the modulator; Γ_c and γ are determined by the optical mode of the fiber and the cross sectional geometry of the EAM, and empirically obtained numbers are adopted in this study [68]. The schematic diagram is shown in Figure 24. The absorption coefficient is a function of frequency and the applied electric field across the QW, which is the most important parameter in estimating the performance of the EAM and we obtain this using the model discussed in the previous chapters. The transmission T was calculated with parameters Γ_c, R, γ, and L set to 0.25, 0, 0.2 and 300 μm [68]. After slight fitting, they are fixed for all samples to secure the consistency.

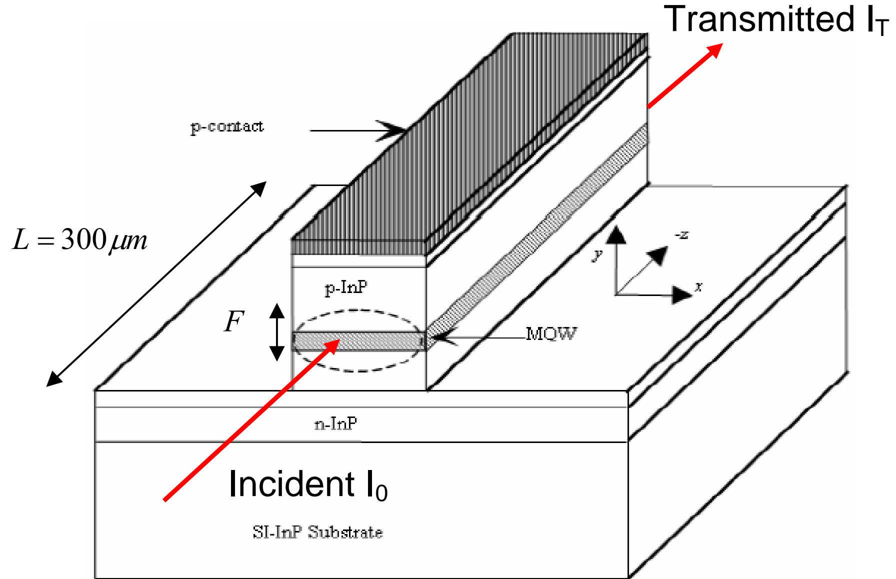

Figure 24. Schematic diagram of an InGaAsP waveguide QW-EAM [68].

5.1.2 Device specifications

We first validate our approach by comparing our results with experimental data available in the literature. The band-edge profiles of the two samples that were experimented are shown in Figure 25. SQW-A is a waveguide EAM whose active region is composed of ten layers of 10.4 nm wide $In_{0.485}Ga_{0.515}As_{0.979}P_{0.021}$ QWs with 7.6 nm thick $In_{0.923}Ga_{0.077}As_{0.325}P_{0.675}$ barriers [67]. SQW-B is the same as SQW-A except for the increased well width of 12 nm and the reduced band offsets from 0.13 (0.163, 0.231) to 0.115 (0.147, 0.212) eV for electron (heavy hole, light hole) [30], which was attempted to achieve higher slope efficiency and higher saturation power compared to those of SQW-

A. As indicated in Ref. [30], the enhanced QCSE due to the increased well width and the shift of the peak of the lowest exciton peak to the higher wavelength did increase the slope efficiency at the expense of the increased insertion loss.

5.1.3 Analysis in Single Quantum Wells

Figure 26 compares the calculated bias-dependent transmission (dB) of SQW-A with the measured data [67], which shows that the two are essentially identical, verifying the validity of the calculation. The calculated absorption spectra of the two samples at low temperature are plotted in Figure 27(a) and (b), showing that the QCSE is enhanced in SQW-B. The bias-dependent FWHM of *cb1-hh1 1s*-like exciton in each sample at 300 K is plotted in Figure 27(e). The FWHM of SQW-B (solid) is slightly smaller than that of SQW-A (dashed) at zero bias because the broadening of energy levels caused by the layer-width fluctuation is less sensitive in the wider well whereas the other contributions are almost identical. As the bias increases, however, the FWHM of SQW-B increases more rapidly because of the higher tunneling probability of the *cb1* state due to the lower barrier height (0.115 eV) and the more rapid increase of Γ_{ww} due to the enhanced QCSE. In both samples, the bias dependence of Γ_T is much stronger than that of Γ_{ww} because of the low conduction-band offsets. As the bias increases from 0 to 150 kV/cm, Γ_{ww} increases from 1.7 to 4.2 and from 1.3 to 4.4 meV in SQW-A and SQW-B, respectively, whereas Γ_T increases from 0 to 8.3 meV and from 0 to 11 meV in the respective samples. The tunneling probability of SQW-B is larger throughout the bias range and increases much faster than that of SQW-A, which guarantees higher optical saturation power of the device. The obtained transmissions of the samples broadened by the FWHMs in Figure 27(e) are plotted in dB as functions of the wavelength and F in (c) and (d).

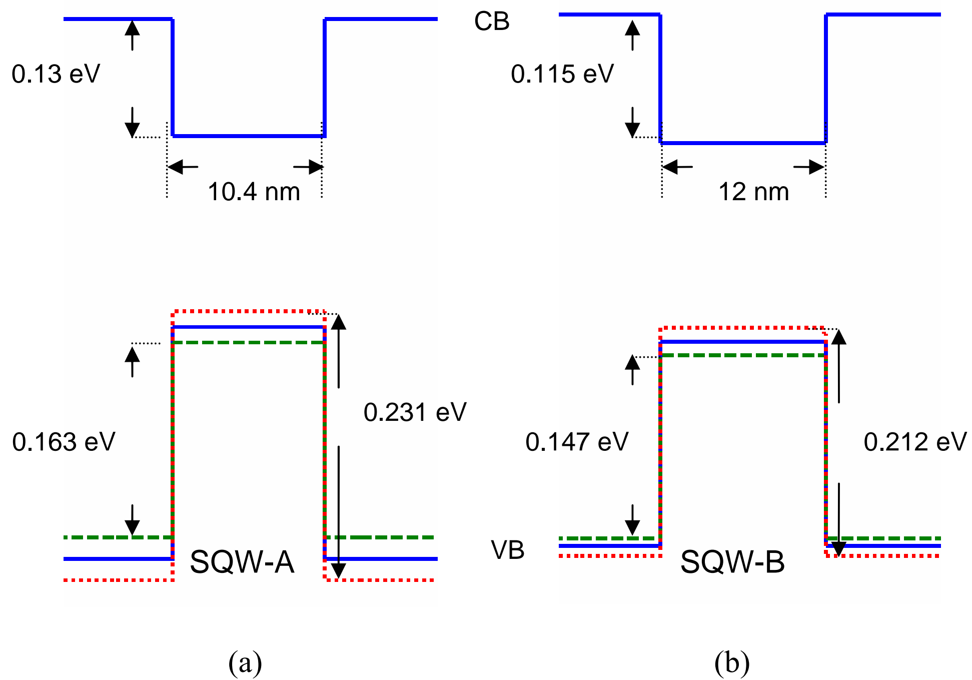

(a) (b)

Figure 25. Band-edge profiles of (a) SQW-A and (b) SQW-B. (Upper solid line: conduction-band edge, lower solid line: valence-band edge with only hydrostatic strain, dotted line: light-hole band edge with shear strain, dashed line: heavy-hole band edge with shear strain). As discussed in Section 2.1.2, the shear components of the strains in the epitaxial layers shifted the effective valence-band edges of heavy (dashed line) and light (dotted line) holes.

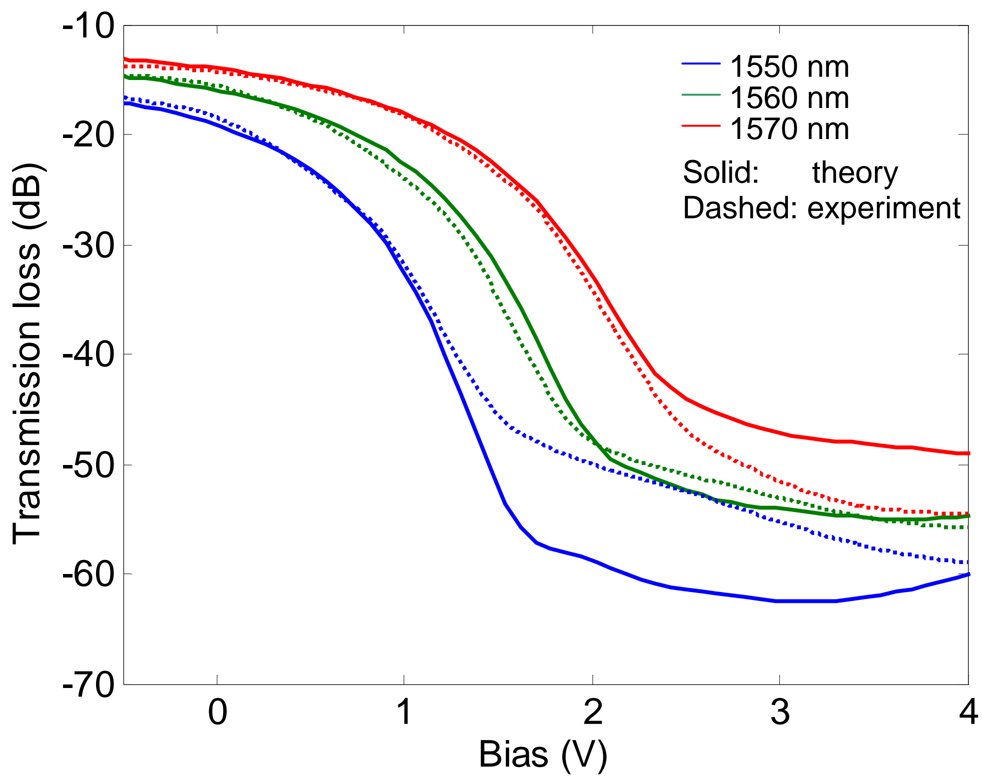

Figure 26. Transmission loss of SQW-A in dB as a function of the applied bias voltage (solid: theory, dashed: experiment) at various wavelengths (from left to right: 1550, 1560, 1570 nm).

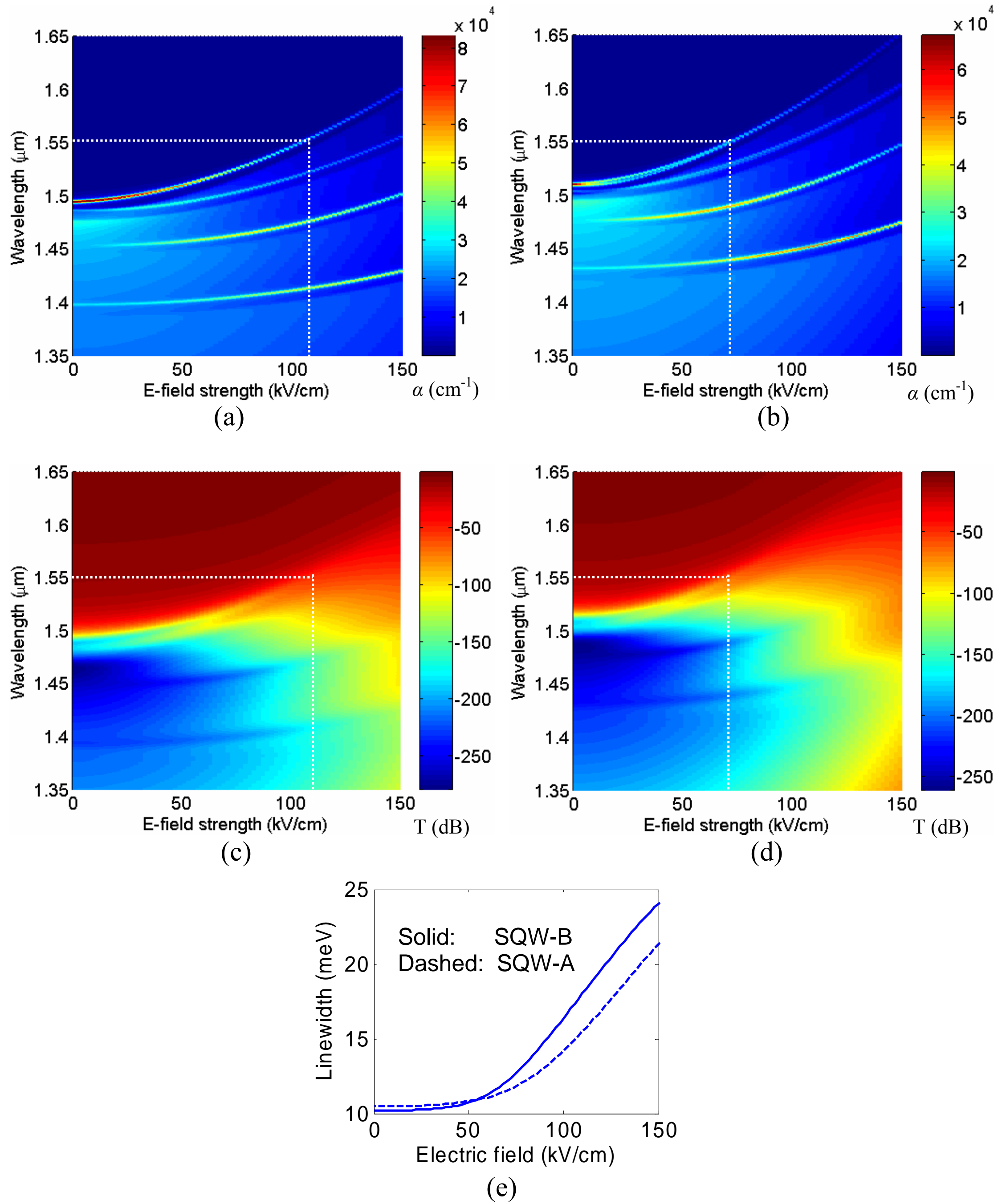

Figure 27. Calculated absorption coefficients of SQW-A (a) and SQW-B (b) as functions of bias and wavelength (FWHM = 1 meV was assumed to observe the peak shift and oscillator strength clearly) and transmission loss in dB of SQW-A (c) and SQW-B (d) at room temperature [bias-dependent FWHM (e) was used for the broadening]. The horizontal dotted lines (1550 nm) meet the lowest exciton peaks at 110 (a) and 73 kV/cm (b) in SQW-A and SQW-B, respectively.

The small-signal modulation efficiency for an analog optical link is governed by the maximum slope efficiency of the modulator [1], which is obtained from the normalized transmission curve. The transmission that is normalized to its maximum value at each wavelength is plotted in Figure 28. The maximum slope efficiencies at 1550 nm are 0.019 and 0.032 $(kV/cm)^{-1}$ for SQW-A and SQW-B at the bias fields of 70 and 38 kV/cm, respectively, showing ~70 % improvement in SQW-B. The transmission in dB is also plotted in Figure 29. At zero bias, SQW-B has ~6 dB more insertion loss than SQW-A due to the shift of the exciton peak to higher wavelength. As the bias field increases, the transmission curve of SQW-B at 1550 nm decreases smoothly down to -70 dB and meets a notch at ~73 kV/cm where the vertical dotted line crosses. This bias point is where the lowest exciton shifts to 1550 nm from that at zero bias, which is found where the vertical (~73 kV/cm) and horizontal (1550 nm) dotted lines cross in Figure 27(b). In SQW-A at 1550 nm, the same phenomenon occurs at ~110 kV/cm with much smaller transmission ~55 dB [see Figure 27(a)], although the notch is not observed because the FWHM is much larger and the oscillator strength is smaller at this bias. At other wavelengths in Figure 29, sudden changes of the transmission curves can be explained exactly the same way. Consequently, at the expense of the increased insertion loss, SQW-B achieved higher slope efficiency, lower operating bias voltage, and more absorption at the turn-off stage, which was experimentally demonstrated.

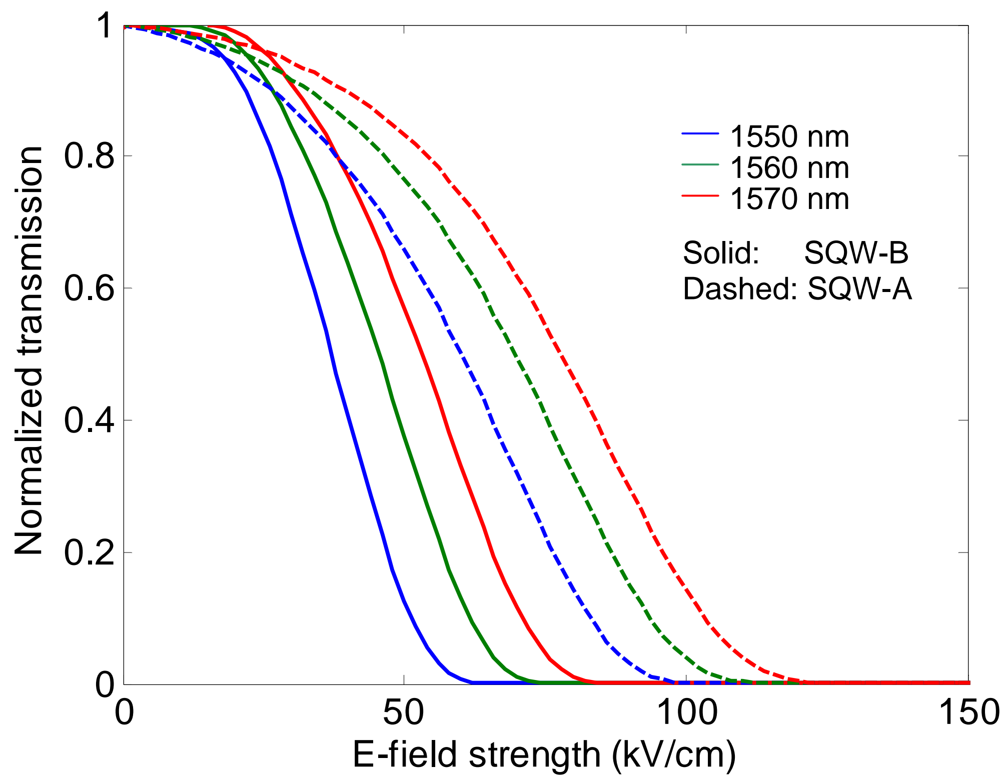

Figure 28. Normalized transmission curves of SQW-A (dashed) and SQW-B (solid) at various wavelengths (from left to right: 1550, 1560, 1570 nm).

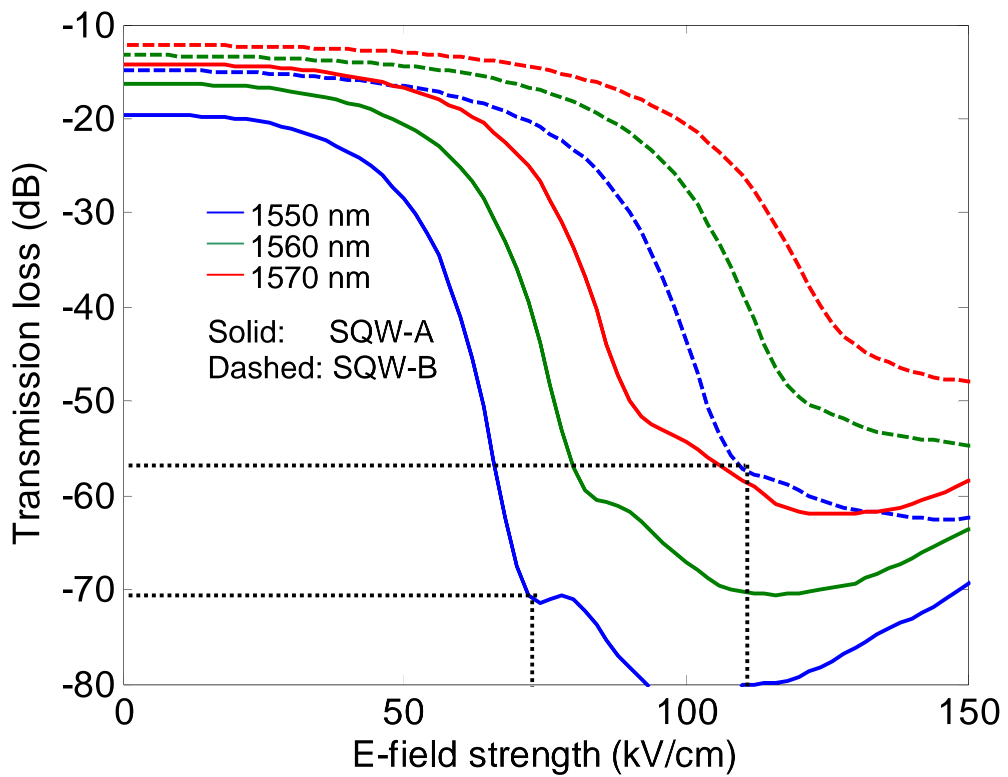

Figure 29. Transmission in dB of SQW-A (dashed) and SQW-B (solid) at various wavelength (from left to right: 1550, 1560, 1570 nm).

5.2 Enhanced slope efficiency in ADQWs

We extend this theoretical analysis to ADQWs and show that the performance of optical EAMs can be improved significantly. To make the problem simple, we fixed all structure and material parameters to those of SQW-A and located a barrier centered at 1.5 nm off the center of the well, where the barrier composition is identical to that of the isolating barrier. The width of the barrier (BW) was varied from 3 to 15 Å with an interval of 3 Å. Clearly, a barrier 3 Å, which is near the half-monolayer thickness, is rather ill-defined in the case of ternaries and quarternaries sharing anions and/or cations, but nonetheless provides a picture of the parameter dependence of the performance. For consistency, the overall bandgap energy of the sample was adjusted to exhibit maximum transmission (insertion loss) of -20 dB at 1550 nm while keeping the conduction- and valence-band-edge profiles unchanged.

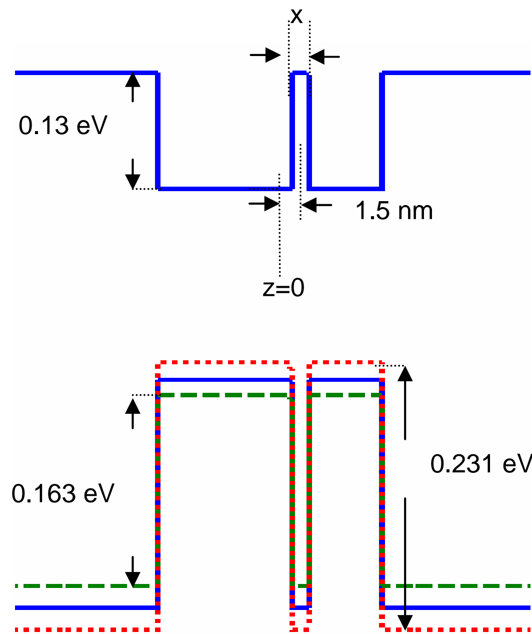

Figure 30. Band-edge profiles of ADQW-x where x denotes the barrier width.

Figure 31 shows the absorption coefficient (a) of the ADQW with 6 Å thick BW at low temperature and the corresponding transmission loss of the EAM (b) that is broadened by the bias-dependent FWHM in Figure 32. At zero bias, most of the *hh1* envelope lies in the wide well, whereas considerable part of *cb1* envelope still remains in the narrow well due to the smaller effective mass and band-offset ratio of the conduction band. As the bias increases from zero, the oscillator strength of the lowest exciton increases and its energy level blue-shifts due to the increased overlap integral of *hh1* and *cb1* envelopes and the corresponding increase of the exciton binding energy until *hh1* subband moves to the narrow well, which we call the critical bias field. Thereafter, a large red-shift is observed due to the rapid reduction of the energy difference between *hh1* (in the narrow well) and *cb1* (in the wide well) subbands while keeping considerable oscillator strength caused by the *cb1* envelope that is remaining in the wide well. The overall bias-dependent line-broadening FWHM of the lowest exciton peak is also minimized at the bias field where the lowest exciton energy is, as shown in Figure 32. At low bias, its bias-dependence is governed by Γ_{ww}, which exhibits an almost linear relation to the slope of the exciton energy level as shown in the inset of Figure 8. At high bias, Γ_T increases rapidly after certain bias field where the Fowler-Nordheim tunneling of the electron in *cb1* subband begins to increase, which dominates the overall broadening. The higher slope of Γ_T at negative bias is caused by the higher *cb1*-subband energy that is confined in the narrow well.

At 1550 nm, the lowest exciton peaks are found at 75 and -60 kV/cm for positive and negative bias, respectively, in Figure 31. The corresponding notch in the transmission

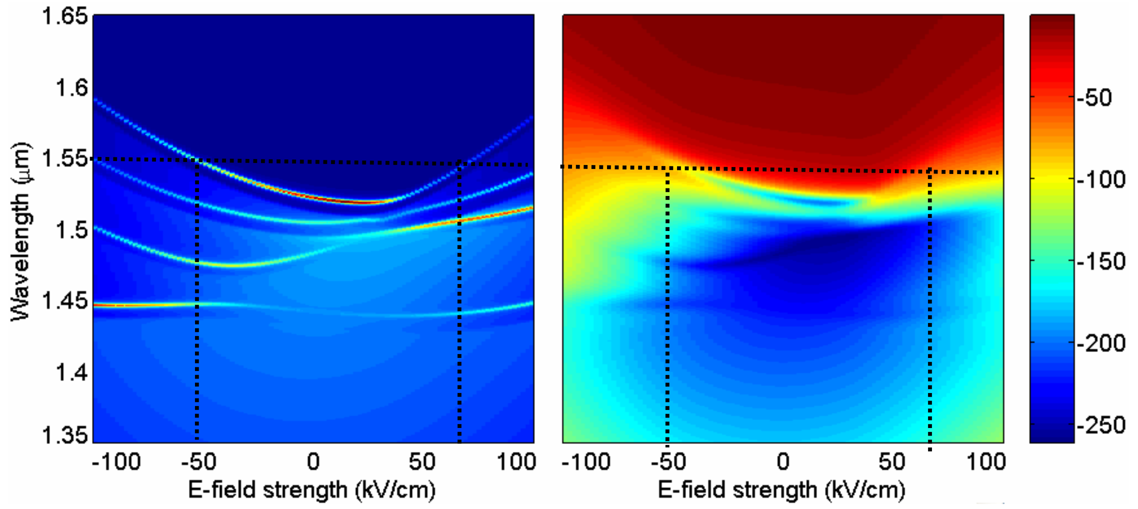

(a) (b)

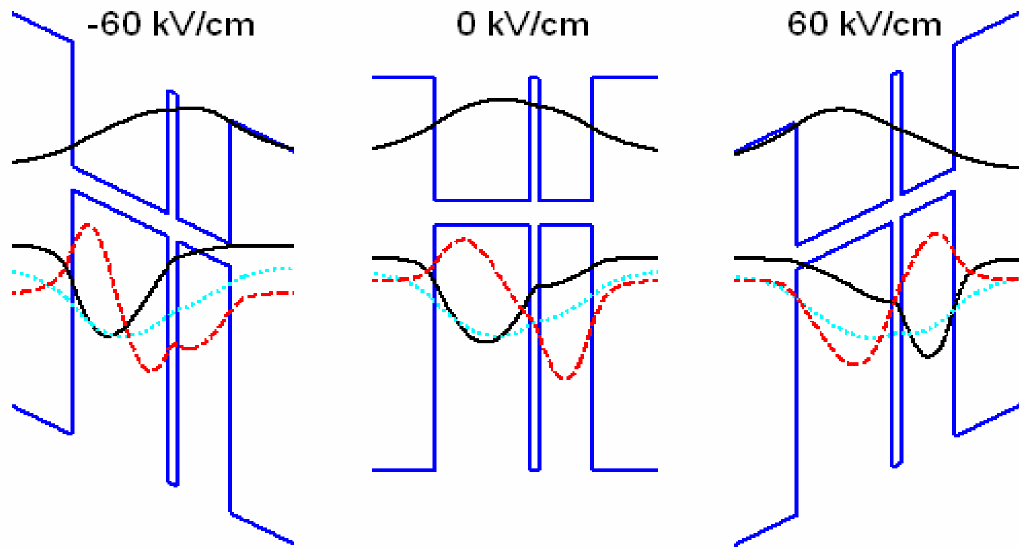

(c)

Figure 31. Calculated absorption coefficients (a) and transmission loss in dB (b) of ADQW-6. The cross points of vertical and dotted lines indicate where the exciton peaks were found at 1550 nm. (c) Band-edge diagrams and envelope functions at $k_{||}=0$ of the lowest electron (*cb1*) and three highest holes (solid: *hh1*, dashed:*hh2*, dotted: *lh1*) under various bias fields.

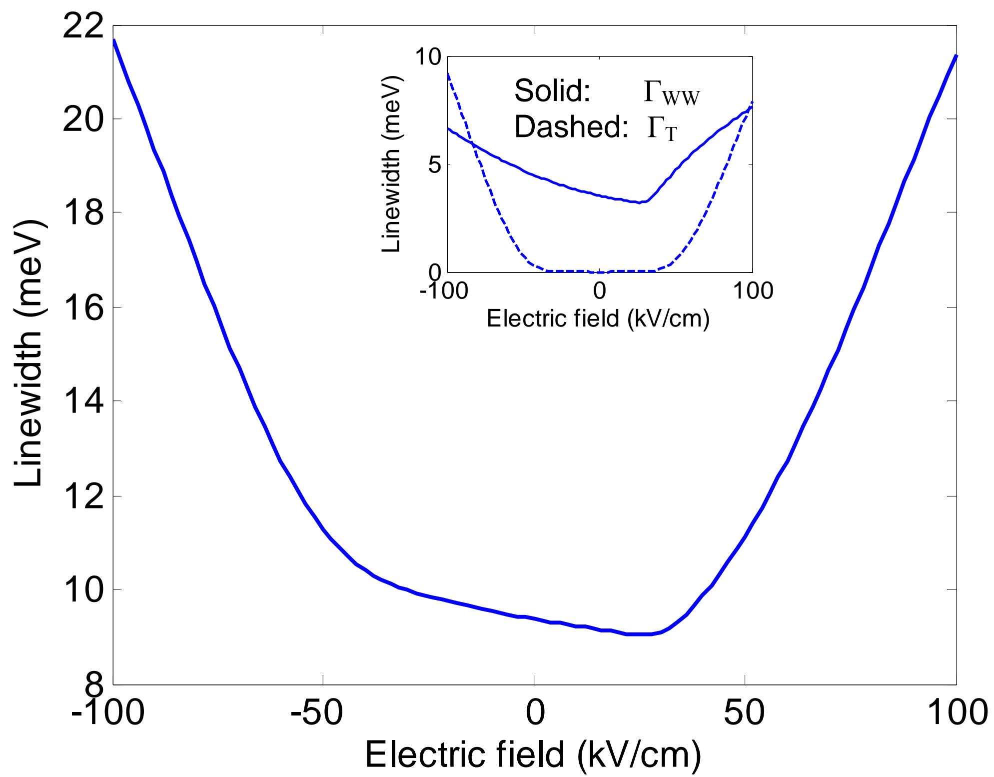

Figure 32. Total line-broadening of ADQW-6 as a function of bias. The inset shows the line-broadening caused by well-width fluctuation (solid) and *cb1*-subband tunneling (dotted).

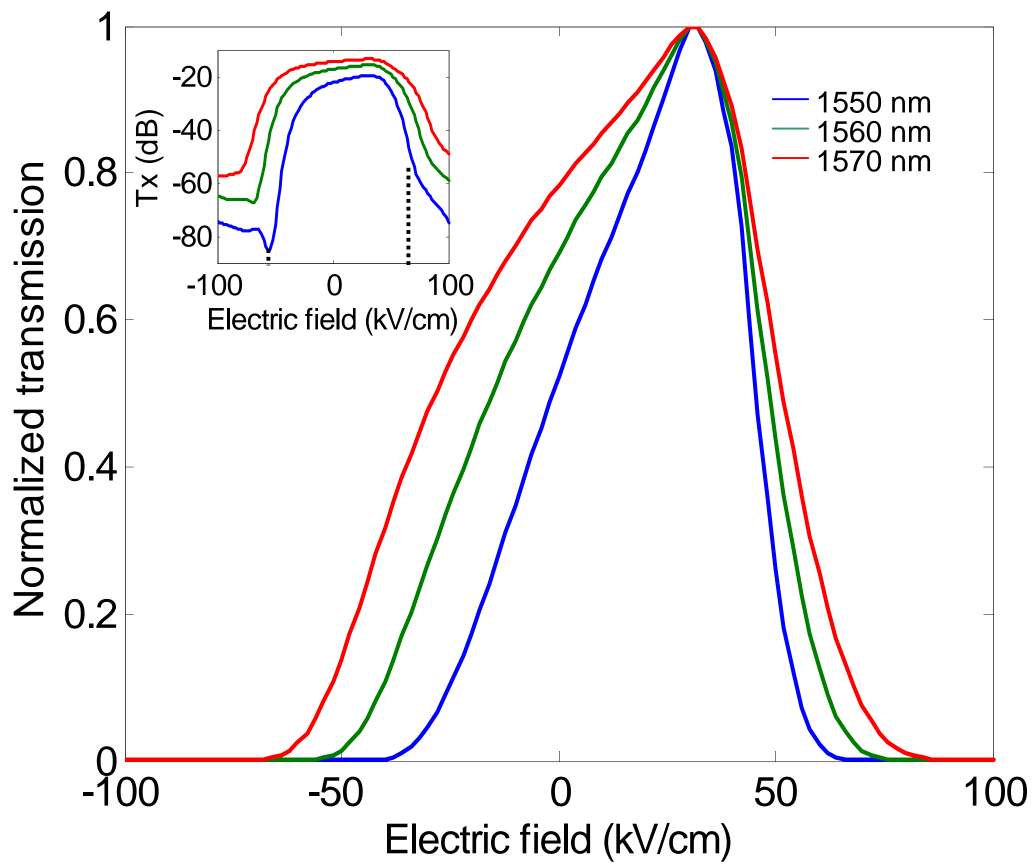

Figure 33. Normalized transmission curves of ADQW-6 at various wavelength (from the center: 1550, 1560, 1570 nm). Inset: transmission in dB of ADQW-6 at various wavelength (from the center: 1550, 1560, 1570 nm).

curve (inset of Figure 33) is, however, not observable at 75 kV/cm because of the same reason that was described for SQW-A. The normalized transmissions at several wavelengths are plotted in Figure 33. The maximum transmission is found at the bias field ~30 kV/cm, following which the transmission falls off rapidly due to the shift of exciton peak and the increased line-broadening. The maximum slope efficiency is observed at ~42 kV/cm.

The maximum slope efficiencies and other important numbers of the five ADQW samples and two SQW samples are summarized in Table I. The slope efficiency of the ADQW with 1.2 nm thick BW (ADQW-12), which showed best performance among the samples, is enhanced by 3.8 times that of SQW-A at a much reduced bias of ~34 kV/cm. The highest extinction ratio is found in ADQW-6 with the minimum transmission at the negative bias of -56 kV/cm although further study is required on this. In ADQWs with barriers thicker than 12 Å, the enhancement begins to decrease mainly because of the diminished oscillator strength of the lowest exciton peak, which is caused by the increased confinement of the *cb1* envelope in the wide well. However, the optimum barrier thickness may change depending on the other structural parameters of the EAM such as interaction length.

Table 1. Comparison of slope efficiencies and other parameters in different QW structures

Sample	Maximum slope efficiency (cm/kV) / bias field (kV/cm)	$T_{dB,max}$ (dB) / bias field	$T_{dB,min}$(dB) / bias field
SQW-A	**0.019** / 70	-15 / 0	-57 / 110
SQW-B	0.032 / 38	-20 / 0	-71 / 72
ADQW-3	0.054 / 44	-20 / 30	-82 / -65
ADQW-6	0.058 / 42	-20 / 30	**-86** / -56
ADQW-9	0.060 / 32	-20 / 28	-85 / -50
ADQW-12	**0.074** / 34	-20 / 28	-81 / -48
ADQW-15	0.068 / 34	-20 / 28	-74 / -46

In summary, there are three main factors that contributed to the enhancement of the slope efficiency exclusively in ADQWs: First, the bias for the maximum transmission moves from that of flat-band condition (zero-field) to substantially higher field, which also reduces the operating bias voltage. Second, after the critical bias, the increased bias-dependent red-shift of the lowest exciton, while retaining a substantial amount of the oscillator strength, increases the transmission loss rapidly. Third, rapid increase of FWHM after the critical bias helps increase the transmission loss even more rapidly by broadening the peak to the operating wavelength.

CHAPTER 6

CONCLUSIONS

In summary, the linear optical properties of the ADQWs were analyzed and the band-edge profile was optimized to exhibit enhanced QCSE leading to improved performances of QW-EAMs. In the calculation of the optical susceptibilities, band-to-band transitions as well as exciton transitions were included, which is based on an accurate exciton model in momentum space, band-edge profiles obtained by a recently developed interpolation scheme, the use of up-to-date material parameters, and a number of material-related line-broadening mechanisms. The mixing effect of excitons originating in different subband pairs in ADQWs was investigated in the range of electric field where the two highest heavy-hole subbands mix strongly in their dispersions. This was found to be very important in accurately estimating the optical properties of and optimizing the band profiles of the ADQWs. The parametric optimization of the ADQWs showed that, in a proper asymmetry, the coupling barrier width is the most critical to the enhancement of the modulation sensitivity. The optical transmission curves of InGaAsP-based QW-EAMs were calculated and found to be essentially identical to the experimental data, which confirmed the reliability of the calculation. Estimation of the ADQW-EAMs showed that the slope efficiency can be enhanced significantly (3.8 times larger than that of SQW-A) at substantially reduced bias voltage by properly optimizing the band structures. It was found that the enhancement in the ADQWs is attributed to the three distinguishing factors that are not expected in SQWs – shift of the maximum

transmission bias, enhanced QCSE after the critical bias, and the increase of FWHM near the critical bias.

Currently, the collaborative research on the enhanced ADQW-EAMs based on the simulation result is under discussion with an experimental group, which will enable the realization of the low cost, high sensitivity optical modulators for analog optical fiber-link or fiber-to-the-home applications. The research is now expanded to the investigation of optical properties of the THz-modulated QWs and optimization of the QWs for sideband generations, which can be used as ultra-high-bandwidth optical switches in the future wavelength division multiplexing systems [39].

APPENDIX A

The theory of the **k·p** method enables one to calculate the band structure of semiconductor. From the one-particle Schrödinger equation in a periodic potential

$$\mathrm{H}\psi_{\lambda} = \left(\frac{p^2}{2m_0} + V_0(\mathbf{r})\right)\psi_{\lambda}(\mathbf{k},\mathbf{r}) = E_{\lambda}(\mathbf{k})\psi_{\lambda}(\mathbf{k},\mathbf{r}),$$

where the wave function is expressed by the Bloch function

$$\psi_{\lambda}(\mathbf{k},\mathbf{r}) = \frac{e^{i\mathbf{k}\cdot\mathbf{r}}}{L^{3/2}}U_{\lambda}(\mathbf{k},\mathbf{r}).$$

The Bloch function, $U_{\lambda}(\mathbf{k},\mathbf{r})$ has the same period as $V_0(\mathbf{r})$. By inserting the wave function into the Schrödinger equation, we get the equation for the Bloch function:

$$\left(\frac{\hbar^2}{2m_0}\nabla^2 + V_0(\mathbf{r}) + [\frac{\hbar^2 k^2}{2m_0} + \frac{\hbar}{m_0}(\mathbf{k}\cdot\mathbf{p})]\right)U_{\lambda}(\mathbf{k},\mathbf{r}) = E_{\lambda}(\mathbf{k})U_{\lambda}(\mathbf{k},\mathbf{r}),$$

which is the starting point of the **k·p** analysis. The resulting Luttinger-Kohn Hamiltonian for the valence band in a bulk semiconductor is

$$H_{LK,0} = \begin{pmatrix} P+Q & L & M & 0 \\ L^* & P-Q & 0 & M \\ M^* & 0 & P-Q & -L \\ 0 & M^* & -L^* & P+Q \end{pmatrix}, \tag{A1-1}$$

where $P = \frac{1}{3}(A+2B)(k_x{}^2 + k_y{}^2 + k_z{}^2)$,

$$Q = \frac{1}{6}(A-B)(k_x{}^2 + k_y{}^2 - 2k_z{}^2),$$

$$L = -\frac{iC}{\sqrt{3}}(k_x - ik_y)k_z$$

$$M = \frac{1}{\sqrt{12}}\left[(A-B)(k_x{}^2 - k_y{}^2) - 2iCk_xk_y\right].$$

The Luttinger parameter γ_1, γ_2, and γ_3 are related to A, B, and C by the relations:

$$\frac{\hbar^2\gamma_1}{2m} = \frac{1}{3}(A+2B),\ \frac{\hbar^2\gamma_2}{2m} = \frac{1}{6}(A-B),\ \text{and}\ \frac{\hbar^2\gamma_3}{2m} = \frac{C}{6}.$$

The corresponding basis functions for the Hamiltonian are

$$U^{\frac{3}{2}}(\mathbf{r}) = \left|\frac{3}{2},\frac{3}{2}\right\rangle = -\frac{1}{\sqrt{2}}(x+iy)\alpha \qquad \text{: heavy hole spin-up}$$

$$U^{\frac{1}{2}}(\mathbf{r}) = \left|\frac{3}{2},\frac{1}{2}\right\rangle = \frac{1}{\sqrt{6}}[-(x+iy)\beta + \sqrt{\frac{2}{3}}z\alpha] \qquad \text{: light hole spin-up}$$

$$U^{-\frac{1}{2}}(\mathbf{r}) = \left|\frac{3}{2},-\frac{1}{2}\right\rangle = \frac{1}{\sqrt{6}}[(x-iy)\alpha + \sqrt{\frac{2}{3}}z\beta] \qquad \text{: light hole spin-down}$$

$$U^{-\frac{3}{2}}(\mathbf{r}) = \left|\frac{3}{2},-\frac{3}{2}\right\rangle = \frac{1}{\sqrt{2}}(x-iy)\beta \qquad \text{: heavy hole spin-down}$$

where, x, y, and z are p-like unit cell Bloch wave functions in the valence band and α and β are the spin-up and spin-down states of the electron. The subband structure for the QWs can be obtained by solving the Schrödinger equation

$$\left[H_{LK,0} + V_h(z)\right]\Psi(z) = E\ \Psi\ (z),$$

where $V_h(z)$ is the valence band-edge profile. The resulting Hamiltonian for the valence band in a QW is

$$H_{LK,QW} = \begin{pmatrix} P+Q+V_h & L & M & 0 \\ L^* & P-Q+V_h & 0 & M \\ M^* & 0 & P-Q+V_h & -L \\ 0 & M^* & -L^* & P+Q+V_h \end{pmatrix},$$

where $P = \frac{\hbar^2 \gamma_1}{2m}\left[k_\parallel{}^2 + (\frac{p_z}{\hbar})^2 \right]$,

$$Q = \frac{\hbar^2 \gamma_2}{2m}\left[k_\parallel{}^2 - 2(\frac{p_z}{\hbar})^2 \right],$$

$$L = \frac{\hbar^2 \gamma_3}{2m}\left[-2\sqrt{3}(k_x + ik_y)\frac{p_z}{\hbar} \right],$$

$$M = \frac{\hbar^2}{2m}\left[-\sqrt{3}\gamma_2 (k_y{}^2 - k_x{}^2) - 2\sqrt{3}\gamma_3 ik_x k_y \right].$$

APPENDIX B

The oscillator strengths of the uncoupled ground-state excitons $f_{11(2)}^{1s,UC}$ are calculated from Eq. (6)

$$f_{11(2)}^{1s,UC} \sim \left| GI_{11(2)}^{1s,UC} \right|^2$$

and their sum $f_{sum}^{1s,UC}$ is

$$f_{sum}^{1s,UC} = f_{11}^{1s,UC} + f_{12}^{1s,UC} \sim \left| GI_{11}^{1s,UC} \right|^2 + \left| GI_{12}^{1s,UC} \right|^2 . \qquad \text{(A2-1)}$$

The application of the almost-degenerate perturbation theory to the two uncoupled ground states yields two mixed states

$$G_{ADP}^{1s,C} = c_1 G_{11}^{1s,UC} + c_2 G_{12}^{1s,UC} \text{ and } G_{ADP}^{2s,C} = c_2 G_{11}^{1s,UC} - c_1 G_{12}^{1s,UC} \ ,$$

where c_1 and c_2 are the elements of the eigenvectors that are obtained by diagonalizing Eq. (9), which are normalized ($c_1^2 + c_2^2 = 1$). From Eq (6), the corresponding oscillator strengths are

$$f^{1s,ADP} \sim \left| c_1 GI_{11}^{1s,UC} + c_2 GI_{12}^{1s,UC} \right|^2 \text{ and } f^{2s,ADP} \sim \left| c_2 GI_{11}^{1s,UC} - c_1 GI_{12}^{1s,UC} \right|^2 .$$

Adding $f^{1s,ADP}$ and $f^{2s,ADP}$ after taking the modulus square yields the same expression as $f_{sum}^{1s,UC}$ in Eq. (A2-1).

REFERENCES

[1] G. L. Li and P. K. L. Yu, “Optical intensity modulators for digital and analog applications,” *J. Lightwave Technol.*, vol. 21, pp. 3011–3019, 2003.

[2] A. Ramdane, A. Ougazzaden, F. Devaux, F. Delorme, M. Schneider, and J. Landreau, “Very simple approach for high performance DFB laser-electroabsorption modulator monolithic integration,” *Electron. Lett.*, vol. 30, pp. 1980–1981. 1994

[3] M. Shinada and S. Sugano, “Interband optical transitions in extremely anisotropic semiconductors. I. Bound and unbound exciton absorption,” *J. Phys. Soc. Jpn.*, vol. 21, pp. 1936–1946, 1966.

[4] R. Dingle, W. Wiegmann, and C. H. Henry, “Quantum states of confined carriers in very thin $Al_xGa_{1-x}As$-GaAs-$Al_xGa_{1-x}As$ heterostructures,” *Phys. Rev. Lett.*, vol. 33, pp. 827–830, 1974.

[5] R. J. Elliott, “Intensity of optical absorption by excitons,” *Phys. Rev.*, vol. 108, pp. 1384–1389, 1957.

[6] R. C. Miller, D. A. Kleinman, W. T. Tsang, and A. C. Gossard, “Observation of the excited level of excitons in GaAs quantum wells,” *Phys. Rev. B*, vol. 24, pp. 1134–1136, 1981.

[7] G. Bastard, E. E. Mendez, L. L. Chang, and E. Esaki, “Exciton binding energy in quantum wells,” *Phys. Rev. B*, vol. 26, pp. 1974–1979, 1982.

[8] R. L. Greene, K. K. Bajaj, and D. E. Phelps, “Energy levels of Wannier excitons in GaAs-$Ga_{1-x}Al_xAs$ quantum-well structures,” *Phys. Rev. B*, vol. 29, pp. 1807–1812, 1984.

[9] C. Priester, G. Allan, and M Lannoo, “Wannier excitons in GaAs-$Ga_{1-x}Al_xAs$ quantum-well structures: Influence of the effective-mass mismatch,” *Phys. Rev.* vol. 30, pp. 7302–7304, 1984.

[10] D. M. Whittaker and R. J. Elliott, “Theory of magneto-exciton binding energy in realistic quantum well structures,” *Solid State Comm.*, vol. 68, pp. 1–5, 1988.

[11] G. D. Sanders and Y.-C. Chang, "Effect of band hybridization on exciton states in GaAs-$Ga_{1-x}Al_xAs$ quantum wells," *Phys. Rev. B*, vol. 32, pp. 5517–5520, 1985.

[12] L. C. Andreani and A. Pasquarello, "Accurate theory of excitons in GaAs-$Ga_xAl_{1-x}As$ quantum wells," *Phys. Rev. B*, vol. 42, pp. 8928–8938, 1990.

[13] S. Jorda, U. Rössler, and D. Broido, "Fine structure of excitons and polariton dispersion in quantum wells," *Phys. Rev. B*, vol. 48, pp. 1669–1677, 1993.

[14] R. Winkler, "Excitons and fundamental absorptions in quantum wells," *Phys. Rev. B*, vol. 51, pp. 14395–14409, 1995.

[15] D. A. B. Miller, D. S. Chemla, T. C. Damen, A. C. Gossard, W. Wiegmann, T. H. Wood, and C. A. Burrus, "Band-edge electroabsorption in quantum well structures: the quantum-confined Stark effect," *Appl. Phys. Lett.*, vol. 53, pp.2173–2176, 1984.

[16] D. F. Blossey and P. Handler, "Electroabsorption," in *Semiconductors and Semimetals*, vol. 9, edited by R. K. Willardson and A. C. Beer, New York and London, Academic Press, 1972.

[17] D. A. B. Miller, D. S. Chemla, T. C. Damen, A. C. Gossard, W. Wiegmann, T. H. Wood, and C. A. Burrus, " Electric field dependence of optical absorption near the band gap of quantum-well structures," *Phys. Rev. B*, vol. 32, pp. 1043–1060, 1985.

[18] G. Bastard, E. E. Mendez, L. L. Chang, and L. Esaki, "Variational calculations on a quantum well in an electric field," *Phys. Rev. B*, vol. 28, pp. 3241–3245, 1983.

[19] T. H. Wood, C. A. Burrus, D. A. B. Miller, D. S. Chemla, T. C. Damen, A. C. Gossard, and W. Wiegmann, "High-speed optical modulation with GaAs/GaAlAs quantum wells in a p-i-n diode structure," *Appl. Phys. Lett.*, vol. 44, pp. 16–18, 1984.

[20] Y. J. Chen, Emil S. Koteles, B. S. Elman, and C. A. Armiento, "Effect of electric fields on excitons in a coupled double-quantum-well structure," *Phys. Rev. B*, vol. 36, pp. 4562–4565, 1987.

[21] S. R. Andrews, C. M. Murray, R. A. Davies, and T. M. Kerr, "Stark effect in strongly coupled quantum wells," *Phys. Rev. B*, vol. 37, pp. 8198–8204, 1988.

[22] J. Lee, M. O. Vassell, Emil S. Koteles, and B. Elman, "Excitonic spectra of asymmetric, coupled double quantum wells in electric fields," *Phys. Rev. B*, vol. 39, pp. 10133–10143, 1989.

[23] C. C. Phillips and R. Eccleston, "Theoretical and experimental picosecond photoluminescence studies of the quantum-confined Stark effect in a strongly coupled double-quantum-well structure," *Phys. Rev. B*, vol. 40, pp. 9760–9766, 1989.

[24] M. K. Chin, "Modeling of InGaAs/InAlAs coupled double quantum wells," *J. Appl. Phys.*, vol. 76, pp. 518–523, 1994.

[25] N. Susa, "Improvement in electroabsorption and the effects of parameter variations in the three-step asymmetric coupled quantum well," *J. Appl. Phys.*, vol. 73, pp. 932–942, 1993.

[26] Y. Tokuda, K. Kanamoto, Y. Abe, and N. Tsukada, "Observation of excitonic effects on electroabsorption in coupled quantum wells," *Phys. Rev. B*, vol. 41, pp. 10280–10282, 1990.

[27] C. Thirstrup, "Refractive index modulation based on excitonic effects in GaInAs-InP coupled asymmetric quantum wells," *IEEE J. Quantum Electron.*, vol. 31, pp. 988–996, 1995.

[28] P. Steinmann, B. Borchert, and B. Stegmüller, "Asymmetric quantum wells with enhanced QCSE: modulation behaviour and application for integrated laser/modulator," *IEEE Photon. Technol. Lett.*, vol. 9, pp. 191–193, 1997.

[29] R. K. Gug and W. E. Hagston, "Enhancement of the quantum-confined stark effect utilizing asymmetric quantum well structures," *Appl. Phys. Lett.*, vol. 74, pp. 254–256, 1999.

[30] B. Liu, J. Shim, Y. Chiu, A. Keating, J. Piprek, and J. E. Bowers, "Analog characterization of low-voltage MQW traveling-wave electroabsorption modulators," *J. Lightwave Technol.*, vol. 21, pp. 3011–3019, 2003.

[31] Y. Zhuang, W. S. C. Chang, and P. K. L. Yu, "Peripheral-coupled-waveguide MQW electroabsorption modulator for near transparency and high spurious free dynamic range RF fiber-optic link," *IEEE Photon. Technol. Lett.*, vol. 16, pp. 2033–2035, 2004.

[32] D. K. Kim and D. S. Citrin, “Electric-field-induced strong mixing between *e1-hh1* and *e1-hh2* excitons in asymmetric double quantum wells,” *Phys. Rev. B*, vol. 76, pp. 125305, Sep. 2007.

[33] H. Haug and S. W. Koch, *Quantum Theory of the Optical and Electronic Properties of Semiconductors*, 3rd ed. Singapore: World Scientific, 1994.

[34] G. P. Donati, R. Kaspi, and K. J. Malloy, “Interpolating semiconductor alloy parameters: Application to quaternary Ⅲ-Ⅴ band gaps,” *J. Appl. Phys.*, vol. 94, pp. 5814–5819, 2003.

[35] I. Vurgaftman, J. R. Meyer, and L. R. Ram-Mohan, “Band parameters for Ⅲ-Ⅴ compound semiconductors and their alloys,” *J. Appl. Phys.*, vol. 89, pp. 5815–5875, 2001.

[36] For the introductory review of the line broadening of optical transitions, see F. T. Vasko and A.V. Kuznetsov, *Electronic States and Optical Transitions in Semiconductor Heterostructures,* New York: Springer, 1999.

[37] D. K. Kim and D. S. Citrin, “Optimized asymmetric double quantum wells for high electric-field-sensitivity electroabsorption: excitonic mixing effects,” *IEEE J. Quantum Electron*., vol. 43, no. 8, pp. 651-654, Aug. 2007.

[38] D. K. Kim and D. S. Citrin, “Electrooptic properties of InGaAsP asymmetric double quantum wells: enhanced slope efficiency in waveguide electroabsorption modulators,” *IEEE J. Quantum Electron*., vol. 43, no. 9, pp. 765-772, Sep. 2007.

[39] D. K. Kim and D. S. Citrin, “1 THz modulation in InGaAsP multiple quantum wells for 40 Gbps applications,” in press, *IEEE J. Sel. Topics Quantum Electron*., vol. 14. no. 2, March/April 2008.

[40] T. H. Glisson, J. R. Hauser, M. A. Littlejohn, and C. K. Willams, “Energy bandgap and lattice constant contour of Ⅲ-Ⅴquaternary alloys,” *J. Electron. Mater.*, vol. 7, pp. 1–16, 1978.

[41] R. L. Moon, G. A. Antypas, and L. W. James, “Bandgap and lattice constant of InGaAsP as a function of alloy composition,” *J. Electron. Mater.*, vol. 3, pp. 635–644, 1974.

[42] S. L. Chuang, "Efficient band-structure calculations of strained quantum wells," *Phys. Rev. B,* vol. 43, pp. 9649–9661, 1991.

[43] T. Kamizato, M. Matsuura, "Excitons in double quantum wells," *Phys. Rev. B,* vol. 40, pp. 8378–8384, 1989.

[44] G. D. Sanders and Y. C. Chang, "Theory of photoabsorption in modulation-doped semiconductor quantum wells," *Phys. Rev. B*, vol. 35, pp. 1300–1315, 1987.

[45] P. Y. Yu and M. Cardona, *Fundamentals of Semiconductors*, New York, NY: Springer-Verlag, Inc., 2003.

[46] S. Hughes, "High-field wave packets in semiconductor quantum wells: A real-space finite-difference time-domain formalism," *Phys. Rev. B*, vol. 69, pp. 205308, 2004.

[47] G. D. Sanders, "Electronic and optical properties of semiconductor quantum wells," PhD dissertation, University of Illinois, Urbana-Champaign, IL, USA, 1985

[48] A. M. Fox, D. A. B. Miller, G. Livescu, J. E. Cunningham, and W. Y. Jan, "Quantum well carrier sweep out: relation to electroabsorption and exciton saturation," *IEEE J. Quantum Electron.*, vol. 27, pp. 2281–2295, 1991.

[49] P. J. Stevens, M. Whitehead, G. Parry, and K. Woodbridge, "Computer modeling of the electric field dependent absorption spectrum of multiple quantum well material," *IEEE J. Quantum Electron.*, vol. 24, pp. 2007–2016, 1988.

[50] D. S. Chemla and D. A. B. Miller, "Room-temperature excitonic nonlinear-optical effects in semiconductor quantum-well structures," *J. Opt. Soc. Am. B*, vol. 2, pp. 1155–1173, July 1985.

[51] O. Madelung, *Semiconductors–Basic Data*, *2nd ed.*, Berlin: Springer–Verlag, 1996.

[52] A. Larsson, P. A. Andrekson, S. T. Eng, and A. Yariv, "Tunable superlattice p-i-n photodetectors: characteristics, theory, and applications," *IEEE J. Quantum Electron.*, vol. 24, pp. 787–801, 1988.

[53] M. Sugawara, T. Fujii, S. Yamazaki, and K. Nakajima, "Optical characteristics of excitons in $In_{1-x}Ga_xAs_yP_{1-y}$/InP quantum wells," *Phys. Rev. B*, vol. 44, pp.1782–1791, 1991.

[54] C. Lin, J. M. Meese, and Y.-C. Chang, "Optical properties of GaAs/$Al_xGa_{1-x}As$ multiple quantum wells versus electric field including exciton transition broadening effects in optical modulators," *J. Appl. Phys.*, vol. 75, pp. 2618–2627, 1994.

[55] V. Savona and R. Zimmermann, "Time-resolved Rayleigh scattering of excitons: Evidence for level repulsion in a disordered system," *Phys. Rev. B,* vol. 60, pp. 4928–4936, 1999.

[56] W. Chen and T. G. Andersson, "Quantum confined Stark shift for differently shaped quantum wells," *Semicond. Sci. Technol*., vol. 7, pp. 828–836, 1992.

[57] M. M. Dignam and J. E. Sipe, "Exciton states in coupled double quantum wells in a static electric field," *Phys. Rev. B*, vol. 43, pp. 4084-4096, 1991.

[58] J. Soubusta, R. Grill, P. Hlídek, M. Zvára, L. Smrčka, S. Malzer, W. Geißelbrecht, and G. H. Döhler, "Excitonic photoluminescence in symmetric coupled double quantum wells subject to an external electric field," *Phys. Rev. B*, vol. 60, pp. 7740–7743, 1999.

[59] M. Aguilar, M. Carrascosa, F. Agullo-Lopez, F. Agullo-Rueda, M. R. Melloch, and D. D. Nolte, "Linear electroabsorption in semi-insulating GaAs/AlGaAs asymmetric double quantum wells," *J. Appl. Phys*. vol. 86, pp. 3822–3825, 1999.

[60] X. Chen, W. Batty, M. P. Earnshaw, D. W. E. Allsopp, and R. Grey, "Electroabsorption in narrow coupled double quantum wells: Coulombic coupling effects," *IEEE J. Quantum Electron*., vol. 34, pp. 1180–1187, 1998.

[61] M. Y. Su, S. G. Carter, M. S. Sherwin, A. Huntington, and L. A. Coldren, "Strong-field terahertz optical mixing in excitons," *Phys. Rev. B*, vol. 67, pp. 125307, 2003.

[62] S. Ristic and N. A. F. Jeager, "Push–pull polarization conversion using novel asymmetric coupled quantum-well structures," *IEEE Photon. Technol. Lett*., vol. 18, 316–318, 2006.

[63] G. E. W. Bauer and T. Ando, "Exciton mixing in quantum wells," *Phys. Rev. B,* vol. 38, 6015–6030, 1988.

[64] A. M. Fox, D. A. B. Miller, G. Livescu, J. E. Cunningham, and W. Y. Jan, "Excitonic effects in coupled quantum wells," *Phys. Rev. B,* vol. 44, pp. 6231–6242, 1991.

[65] L. Viña, R. T. Collins, E. E. Mendez, and W. I. Wang, "Excitonic coupling in GaAs/GaAlAs quantum wells in an electric field," *Phys. Rev. Lett*., vol. 58, pp. 832–835, 1987.

[66] M. V. Marquezini, J. Tignon, T. Hasche, and D. S. Chemla, "Refractive index and absorption of GaAs quantum wells across excitonic resonances," *Appl. Phys. Lett.*, vol. 73, pp. 2313–2315, 1998.

[67] S. Z. Zhang, Y. Chiu. P. Abraham, and J. E. Bowers, "25-GHz polarization-insensitive electroabsorption modulators with traveling-wave electrodes," *IEEE Photon. Technol. Lett.*, vol. 11, pp. 191–193, 1999.

[68] J. Piprek, Y. Chiu, J. E. Bowers, "Analysis of multi-quantum well electroabsorption modulators," in *Proceedings of SPIE*, vol. 46, pp. 609–617, 2002.